Dating the Broken Hill (Zambia) skull, and its position in human evolution

Rainer Grün[1,2], Alistair Pike[3], Frank McDermott[4], Stephen Eggins[2], Graham Mortimer[2], Maxime Aubert[5,2], Lesley Kinsley[2], Renaud Joannes-Boyau[6,2], Michael Rumsey[7], Christiane Denys[8], James Brink[9], Tara Clark[1,10, 11], Chris Stringer[12]

[1]Australian Research Centre for Human Evolution, Griffith University, Nathan QLD 4111, Australia

[2]Research School of Earth Sciences, The Australian National University, Canberra ACT 2600, Australia

[3]Faculty of Humanities, University of Southampton Avenue Campus, Highfield Southampton SO17 1BF, UK

[4]UCD School of Earth Sciences, University College Dublin, Belfield, Dublin 4, Ireland

[5]Australian Research Centre for Human Evolution & Griffith Centre for Social and Cultural Research, Griffith University, Gold Coast QLD 4222, Australia

[6]Geocscience, Southern Cross University, Lismore NSW 2480, Australia

[7]Department of Earth Sciences, Natural History Museum, London SW5 7BD, UK

[8]Institut de Systématique, Evolution, Biodiversité (ISYEB), Muséum national d'Histoire naturelle, CNRS, Sorbonne Université, EPHE, Université des Antilles, 75231 Paris Cedex 05, France.

[9]Florisbad Quaternary Research, National Museum, P.O. Box 266, Bloemfontein 9300, RSA & Centre for Environmental Management, University of the Free State, Bloemfontein, RSA

[10]School of Earth and Environmental Sciences, University of Queensland, St Lucia QLD 4072, Australia

[11]School of Earth, Atmospheric & Life Sciences, University of Wollongong, Wollongong, NSW 2522, Australia

[12]CHER, Department of Earth Sciences, Natural History Museum, London SW5 7BD, UK

The Broken Hill (Kabwe) cranium was recovered from cave deposits in 1921, during metal ore mining in what is now Zambia. It is one of the best preserved fossil hominins, and was initially designated as the type specimen of *H. rhodesiensis*, but recently it has often been referred to the taxon *H. heidelbergensis*. However, the original site has since been completely quarried away, and although the age of the cranium is often estimated at ~500ka, its unsystematic recovery impedes its accurate dating and its placement in human evolution. Our

analyses carried out directly on the skull yielded a best age estimate of 299±25 ka (2σ). The result suggests that later Middle Pleistocene Africa contained multiple contemporaneous hominin lineages, *H. sapiens, H. heidelbergensis/rhodesiensis and Homo naledi*, similar to Eurasia with *H. neanderthalensis*, 'Denisovans', *H. floresiensis, H. luzonensis* and perhaps also *H. heidelbergensis* and *H. erectus*. The age estimate also adds further questions about the mode of evolution of *H. sapiens* in Africa, and whether *H. heidelbergensis/rhodesiensis* was a direct ancestor for our species.

The Broken Hill (Kabwe) skull (Natural History Museum (NHM) registration number E686, Figure 1), discovered in 1921, was the first important human fossil found in Africa. It was recovered from deposits that were being quarried away during metal ore mining, in what is now Zambia (then Northern Rhodesia). Initially designated the type specimen of *H. rhodesiensis*[1], many workers have recently classified it with fossils such as Petralona and Bodo 1 as *H. heidelbergensis*, a Middle Pleistocene species of Europe and Africa[2-4]. Its age has remained uncertain beyond a probable assignment to the Middle Pleistocene. Here, we estimate its age using radiometric dating methods and show how a relatively young date for the fossil impacts our understanding of the tempo and mode of modern human origins.

Extended Data Figure 1 shows pictures of the skull shortly after it was discovered. Its general find position was summarised by the drawing originally published in the *Illustrated London News* (Extended Data Figure 2). The skull was supposedly found at the base of the "Bone Cave", which was first described by White[5] (Extended Data Figure 3). However, taking account of all descriptions and analytical results (see discussion in the Method Section), it seems unlikely that the skull and the micro-mammal rich sediment, in which it was found, formed the base of the Bone Cave. Instead, it seems more likely that a section of the upper part of the sedimentary deposits, including the skull, was displaced by the mining operation (Extended Data Figure 4).

Subsequent to the discovery of the skull, other fossil human remains were recovered in the site and around the locality, including on spoil heaps, along with various faunal remains and artefacts[6]. However, only the tibia (E691) and femur midshaft fragment (EM 793), discovered the next day, were definitely found in the vicinity of the skull, along with a mineralised calcitic deposit, mistakenly interpreted by some of the miners as a hide (mummified skin). Additionally, some of the microfauna recovered within and around the skull was also saved.

For this paper, the following human skeletal elements were analysed: the skull (E686), the femur head (E907), the femur midshaft (EM793), the tibia (E691) and the partial pelvis (E719) (Extended Data Figure 5). Tibia E691 represents an individual of linear but quite robust build[7] and it has been suggested to represent the same individual as the E686 skull. The femoral midshaft is robust but displays a somewhat modern-looking cross-sectional shape. Similarly mixed archaic and modern features have been discerned in the other unassociated femoral fragments from Broken Hill, which have rather short necks with high neck angles, but they also retain considerable cortical bone. However, one of two separate os coxae from Broken Hill (E719) has a very thick acetabulocristal buttress, comparable with those found in the archaic fossils KNM-ER 3228, Olduvai Hominid 28 (both often attributed to *H. erectus*) and Arago 44 (*H. heidelbergensis*?)[8]. The E687 maxilla appears more *sapiens*-like than E686. It has more canine fossa development than E686, but is large in overall dimensions, resembling the Laetoli Hominid 18 fossil (archaic *H. sapiens*?)[8].

Because of poor provenancing, the Broken Hill material has been difficult to date, and the site has since been completely destroyed by quarrying. Early assessments placed the whole assemblage of human fossils, fauna and artifacts in the late Pleistocene, but more recently, faunal comparisons made with sites such as Olduvai and Elandsfontein have suggested a middle Pleistocene age, perhaps as old as 500 ka[9,10]. However, the limited (and poorly associated) archaeological materials have consistently been attributed to the later Pleistocene/early Middle Stone Age[11-14].

Our re-analyses of the macro and microfauna were inconclusive (see Methods section). The macrofauna probably postdates the end-Cornelian at about 600 ka, even though it seems to contain archaic-looking survivors of earlier periods. The microfauna indicates an age range of between about 300 to 480 ka. Comparing these biostratigraphic assessments with the archaeology, it is difficult to build a coherent picture of the age of the assemblages beyond inferring that they cover a wide time range, with the possibility that the main bone accumulation was relatively earlier in the Middle Pleistocene, while the main human presence (as indicated by the predominant early Middle Stone Age affinities of the artefacts) was later. The small mammal accumulations, according to several drawn sections (e.g. Extended Data Figure 3), were high in the stratigraphy and this may explain the younger biostratigraphic age for the microfauna associated with the skull.

The U-series results are summarised in Figure 2. All samples have high $^{234}U/^{238}U$ activity ratios, between about 2.5 and 4.8, and yield finite closed system U-series results. Uranium sources can be characterised by their initial $^{234}U/^{238}U$ ratios ($^{234}U/^{238}U_i$). While the measured $^{234}U/^{238}U$ ratios of the different parts of the skull are divergent (see Figure 2A), the initial $^{234}U/^{238}U_i$ activity ratios are the

same within error (Extended Data Table 6) indicating that the geochemical environments and U-sources were very similar. All other human skeletal elements were exposed to different U-sources, i.e. they acquired their U in distinct geochemical environments, and at different times to the skull. The U-series ages must be regarded as minimum age estimates as there may be an initial burial time with little or no U-uptake[15]. In the following, we only refer to closed system age estimates. We need to emphasise that apart from the sediment and the small mammals that were collected from around and within the skull, none of the materials collected from the Broken Hill site can unequivocally be connected to the depositional history of the skull, nor can we think of an additional dating analysis to independently verify our results.

Three domains of the skull were analysed for U-series isotopes. Firstly, the dentine attached to the tooth enamel fragments that were used for ESR (see below) was analysed by thermal ionisation mass spectrometry (TIMS, Extended Data Table 3). Secondly, the volumes close to the inner and outer surfaces of a detachable basioccipital fragment were analysed by laser ablation ICP-MS (Extended Data Tables 4 to 6). The means of the isotope values and their errors yield 298±34 ka for the analyses of the inside surface volume and 301±37 ka for the outside surface volume. The weighted mean of these two results gives 299±25 ka as the best estimate for the U-uptake event of the basioccipital fragment. This is 83±25 ka older than the result from the dentine, which can be either explained by a delayed start of the U-uptake into the dentine, or that the dentine stayed an open system for longer[15].

The other human skeletal elements, as well as the calcitic crust, yielded U-series results that are very different from the skull (Figures 2A, B) and acquired their uranium mainly during Marine Isotope Stage (MIS) 6 (i.e. ~191 to 130 ka). Their results are further discussed in the Methods Section but have no bearing on the age assessment of the skull E686. The small mammal bones inside and outside the skull form two clusters between about 100 to 150 ka, one bone being much older (Figure 2B) indicating mixing of different sediment sources. The small mammal bones also had a geochemical environment distinctively different from the skull, i.e. they could not have acquired their uranium whilst inside the skull. This could either mean that the association of the skull with the sediment took place after the microfauna had become a closed system, or that the microfauna was incorporated into the sediment at a later stage. Extended Data Figure 1 shows that the bulk of the sediment is only loosely attached to the skull, and the eye cavities were mainly empty. However, we cannot be certain whether the skull cavity was completely filled with sediment or whether it was more or less empty when found. To conclude, we cannot be sure that the sediment in which the skull was found was actually associated with the skull for any considerable period of

its burial history. The only directly associated sediment remnant we could find after several years of searching was retained during the cleaning operation of the skull in 1921 (Extended Data Figure 11).

ESR analyses were carried out on three tooth enamel fragments. Although it is not possible to calculate a direct ESR age estimation (because of the unknown geological environment of the skull), ESR can be utilised to constrain possible upper age limits. Using the sediment scraped off the skull (Extended Data Figure 11), a combined U-series-ESR calculation yields an upper 2σ age limit of 322 ka (see Methods section for details of the ESR calculations). When modeling dose rate distribution models using a variety of materials from the Broken Hill site (Extended Data Tables 11, 13, Extended Data Figure 12) most calculated upper age limits are significantly younger than 322 ka. Only extreme scenarios would allow older age estimates. Thus we conclude that the age of the skull E686 age is most likely within the error envelope of the closed system U-series age of 299±25 ka.

Implications of the new age estimate for the Broken Hill skull

The result of 299±25 ka for the age of skull E686 has major implications for reconstructions of both behavioural and biological human evolution in Africa. Placing the Broken Hill human fossils later in time suggests caution about inferring the presence of modern humans from the presence of early Middle Stone Age artefacts, both because such archaeological material has been recovered from Broken Hill[11-14], and because the newly estimated ages of the Broken Hill human fossils are within the time range of the early Middle Stone Age[16]. Thus, we can no longer assume that only *Homo sapiens* produced stone tools assigned to the Africa Middle Stone age.

The implications are even more profound for studies of human evolution. E686 has been seen by many workers as part of a relatively gradual and widespread evolutionary sequence in Africa from archaic humans (*H. heidelbergensis*/*H. rhodesiensis*) to modern *H. sapiens*[17,18], with a much older age often estimated at ~500 ka[9,10,18]. Given that fossil material from Omo Kibish and Herto (Ethiopia) assigned to anatomically modern *H. sapiens* has been dated to between 160 and 195 ka[18-20], the fossil record would thus be expected to show a succession of fossils ranging from more archaic at around 500 ka to more modern-looking by about 200 ka. Although the new age determination for the Broken Hill skull lies at a date when an intermediate morphology might be expected, the skull shows no significant anatomically modern derived traits[4].

Another evolutionary scenario is that the roots of *Homo sapiens* are much older than the age estimates for Omo Kibish 1 and Herto, which is supported by age estimates of >200 ka for the fossils from Florisbad (South Africa)[21] and Guomde (Kenya)[22], and of ~300 ka for the Jebel Irhoud (Morocco) material[16,23], all of which display more "modern" traits than E686. In this scenario, Africa contained considerable, perhaps even multispecies skeletal variation around 300 ka, something that is also suggested by age estimates of ~285 ka for the morphologically primitive *Homo naledi* material from South Africa[24,25]. This diversity is consistent with ideas that the evolution of *H. sapiens* was pan-African, taking place via intermittent genetic connections between subdivided populations in different areas of the continent[26]. Such diversity might even have included gene flow between populations that would normally be considered distinct species. Hence, late surviving populations of *Homo heidelbergensis/rhodesiensis* could have been the source of "ghost" introgressions[27].

Thus, just as Eurasia in the later Middle Pleistocene contained the multiple evolving lineages of *H. neanderthalensis*, 'Denisovans', *H. floresiensis, H. luzonensis* and perhaps also *H. heidelbergensis* and *H. erectus*[28], different human lineages/species also co-existed across Africa. As well as the recently identified *H. naledi*, these included late *H. heidelbergensis*/*H. rhodesiensis* as represented by the Broken Hill skull, and early *H. sapiens*, as represented by fossils such as Jebel Irhoud, Florisbad and Guomde. The supposed status of *H. heidelbergensis*/*H. rhodesiensis* as an ancestral species for *H. sapiens* must also be reconsidered in the light of recent studies of the Sima de los Huesos material from Atapuerca, Spain. This sample, which displays clear Neanderthal affinities in both morphology and ancient DNA, has been dated to ~430 ka, suggesting that the evolutionary divergence of *H. neanderthalensis* and *sapiens* took place at a much earlier date[29]. Moreover, new studies of facial evolution also suggest that *H. heidelbergensis*/*H. rhodesiensis* does not represent the most parsimonious last common ancestor[30,31].

References

1. Woodward, A.S., 1921. A new cave man from Rhodesia, South Africa. *Nature* 108**,** 371–372.

2. Stringer, C.B., 1983. Some further notes on the morphology and dating of the Petralona hominid *Journal of Human Evolution* 12, 731-742

3. Stringer, C. 2012. The status of *Homo heidelbergensis* (Schoetensack 1908). *Evolutionary Anthropology* 21, 101–107.

4. Rightmire, G.P., 2017. Middle Pleistocene *Homo* Crania from Broken Hill and Petralona: Morphology, Metric Comparisons, and Evolutionary Relationships. In *Human Paleontology and Prehistory*. Springer International Publishing, Dordrecht, pp. 145–159.

5. White, F., 1908. Notes on a cave containing fossilized bones of animals, worked pieces of bone, stone implements, and quartzite pebbles, found in a kopje or small hill composed of zinc and lead ores, at Broken Hill, North-Western Rhodesia. *Proceedings of the Rhodesian Scientific Association* 7, 13-21.

6. Oakley, K.P., Campbell, B.G., Molleson, T.I., 1977. *Catalogue of Fossil Hominids, Part I: Africa*. London: Trustees of the British Museum, Natural History

7. Trinkaus E. 2009 The human tibia from Broken Hill, Kabwe, Zambia. *PaleoAnthropology* 2009, 145–165

8. Stringer, C.B., 1986. An archaic character in the Broken Hill innominate E 719. *Am. J. phys. Anthrop.* 71, 115–120.

9. Millard, A.R., 2008 A critique of the chronometric evidence for hominid fossils: I. Africa and the Near East 500-50 ka. *Journal of Human Evolution* 54, 848-874.

10. Klein, R. G. 2009. *The human career: human biological and cultural origins*. University of Chicago Press.

11. Clark, J.D.,Oakley, K.P., Wells, L.H., McClelland, J.A., 1947. New studies on Rhodesian Man. *Journal of the Royal Anthropological Institute* 77, 7-32

12. Clark, J.D., 1959. Further excavations at Broken Hill, Northern Rhodesia. *Journal of the Royal Anthropological Institute* 89, 201-232.

13. McBrearty, S., Brooks, A.S., 2000. The revolution that wasn't: a new interpretation of the origin of modern human behaviour. *Journal of Human Evolution* 39, 453-563.

14. Barham, L., Pinto A., Stringer, C., 2002. Bone tools from Broken Hill (Kabwe) cave, Zambia, and their evolutionary significance. *Before Farming* 2002/2.

15. Grün, R., Eggins, S., Kinsley, L., Mosely, H., Sambridge, M., 2014. Laser ablation U-series analysis of fossil bones and teeth. *Palaeogeography, Palaeoclimatology, Palaeoecology* 416, 150-167.

16. Richter D, Grün R, Joannes-Boyau R *et al*. 2017. The age of the hominin fossils from Jebel Irhoud, Morocco, and the origins of the Middle Stone age. *Nature* 546, 293–296.

17. Stringer C., 2002. Modern human origins - progress and prospects. *Philosophical transactions of the Royal Society, London (B)* 357, 563-579

18. White, T.D., Asfaw, B., Degusta, D., Gilbert, H., Richards, G.D., Suwa, G., Clark Howell, F. 2003. Pleistocene *Homo sapiens* from Middle Awash, Ethiopia. *Nature.* 426, 742–747.

19. McDougall, I., Brown, F.H., Fleagle, J.G., 2005. Stratigraphic placement and age of modern humans from Kibish, Ethiopia. *Nature* 433, 733-736.

20. Aubert, M., Pike, A.W.G., Stringer, C., Bartsiokas, A., Kinsley, L., Eggins, S., Day, M., Grün, R., 2012. Confirmation of a late middle Pleistocene age for the Omo Kibish 1 cranium by direct uranium-series dating. *Journal of Human Evolution* 63, 740-710.

21. Grün, R., Brink, J.S., Spooner, N.A., Taylor, L., Stringer, C.B., Franciscus, R.G., Murray, A.S., 1996. Direct dating of Florisbad hominid. *Nature* 382, 500-501.

22. Bräuer, G., Yokoyama, Y., Falguères, C. & Mbua, E. 1997. Modern human origins backdated. *Nature* 386, 337–338.

23. Hublin J-J, Ben-Ncer A, Bailey SE *et al*. 2017. New fossils from Jebel Irhoud, Morocco and the pan-African origin of *Homo sapiens. Nature* 546, 289–292.

24. Berger LR, Hawks J, Dirks PH *et al.* 2017. *Homo naledi* and Pleistocene hominin evolution in subequatorial Africa. *eLife* 6, e24234.

25. Dirks PHGM, Roberts EM, Hilbert-Wolf H, *et al.* 2017. The age of *Homo naledi* and associated sediments in the Rising Star Cave, South Africa. *eLife* 6, e24231.

26. Scerri EML, Thomas MG, Manica A *et al.* 2018. Did our species evolve in subdivided populations across Africa, and why does it matter? *Trends in Ecology & Evolution* 33, 582-594.

27. Lorente-Galdos, B. et al. 2019. Whole-genome sequence analysis of a Pan African set of samples reveals archaic gene flow from an extinct basal population of modern humans into sub-Saharan populations *Genome Biology* 20, Article number 77.

28. Galway‐Witham, J, et al. 2019. Aspects of human physical and behavioural evolution during the last 1 million years. *Journal of Quaternary Science* 34, 355-378

29. Meyer, M. *et al.* 2016. Nuclear DNA sequences from the Middle Pleistocene Sima de los Huesos hominins. *Nature* 531, 504-507.

30. Stringer C B. 2016. The origin and evolution of *Homo sapiens. Philosophical Transactions of the Royal Society B* 371 2015.0237.

31. Lacruz , R.S., Stringer, C.B., W.H., Wood, B., *et al*., 2019. The evolutionary history of the human face. *Nature Ecology & Evolution* 3, 726-736.

32. Ludwig, K.R. 2012. Excel Isoplot add-in. version 3.76.12.02.24.

Figure Captions

Figure 1: The Broken Hill cranium (E686), discovered at the Broken Hill mine, Zambia, in 1921. A: Lateral view. B: Frontal view

Figure 2: (A) U-series results on the human bones. All data points are average age estimates with 2-standard deviations[32]. Dentine: single sample (n=1), (Extended Data Table 3). Skull: laser ablation measurements of basioccipital fragment (for locations see extended data Figure 9A). Outside: (n=4) laser ablation depth profiles each were averaged for the calculation of the $^{230}Th/^{238}U$ and $^{234}U/^{238}U$ isotope ratios and resulting age (Extended Data Tables 4, 5, 6). Inside: (n=3) laser ablation depth profiles were averaged for the $^{234}U/^{238}U$ isotope ratio and (n=8) for the $^{230}Th/^{238}U$ isotope ratio and resulting age (Extended Data Tables 4, 5, 6). Tibia: the average of (n=2) laser ablation cross sections (Extended Data Table 9). Femur midshaft: results of (n=5) individual TIMS measurements (Extended Data Table 3) and (n=1) averaged laser ablation cross section (Extended Data Table 7). Femur head: single (n=1) TIMS analysis (Extended Data Table 3). Pelvis: single (n=1) TIMS analysis (Extended Data Table 3).

(B) U-series results on the small mammal bones found in and around the cranium as well as a calcitic crust found in the vicinity of the cranium. All data points are average age estimates with 2-standard deviations (using the excel isoplot addin, version 3.76.12.02.24). (N=8) bones were analysed from inside the skull, (n=5) with single laser ablation profiles, (n=3) with (n=2) laser ablation depth profiles (Extended Data Table 10). (n=10) bones came from the sediment surrounding the skull, each bone was analysed twice (n=2) (Extended Data Table 10). (n=1) bone was analysed with TIMS (Extended Data Table 3). (n=2) samples of the calcitic layers were analysed (Extended Data Table 3)

METHODS

1. Location of the skull. For the subsequent analyses and their interpretation, it is important to try to reconstruct the burial history of the skull. Various photos taken shortly after the skull was found are shown in Extended Data Figure 1. The general position of the skull find was summarised by the drawing originally published in the *Illustrated London News* (Extended Data Figure 2). The skull was found at the very base of the so-called Bone Cave, which was first described by White[33]. During the mining operations various parts of the cave were exposed at different times and its composite was summarised by Harris[34] (see Extended Data Figure 2) and Clark *et al.*[35]. The cave consisted of two sections, a slightly dipping upper cave, about 40 to 50 m long running from west to east. At about 3 m below the dry season water table, the lower cave took a steep dip and was filled to the roof. At 12 to 15 m below the surrounding surface, the walls disappeared and some bones occurred in a matrix of soft, friable lead carbonate. Some distance beneath that ore, the skull was found embedded in detrital material, which was not mineralised, and contained the bones of small mammals.

There are conflicting views concerning at what depth the skull was found (60 or, more consistently quoted, 90 feet below general ground level; both depths are given[36] (p 103 and various others[36]), where the water table was (during the wet season at one or two feet below the surrounding surface and -18 feet during the dry season[33], or at about -15 and -30 feet, respectively[35]), and at which height the entrance was (at ground level[34] or well above[35]).

There are also differing reports about whether the skull was found with other skeletal remains of the same individual, the latter being removed and smelted, or whether the skull was covered by a supposedly petrified 'hide', or whether this was found nearby. Considering all reports, we agree with the conclusion of Hrdlička[36] that the report of the person who found the skull, Tom Zwigelaar, is the most reliable. Hrdlička had travelled in 1926 to the quarry and interviewed most of the people involved in the find, the discovery of putatively associated materials, and the subsequent transport to what was then the British Museum (Natural History) in London. Zwigelaar is reported saying[36]: "*...we were "hand picking" in a pocket where there was much lead ore. The digging was not hard, not like stone, more loose. After one of the strokes of the pick some of the stuff fell off, and there was the skull looking at me..... The skull was at some depth under the pure lead ore and, as far as I can recall, about 10 feet below what seemed to be the floor of the bone cave further away…..There were no other bones close or near to the skull, and no other objects that arose attention. But a little later and not far below the skull we came on a sort of bundle which looked like the flattened roll of*

hide standing nearly upright; it showed no remains of a real hide but looked somewhat like it. Pieces of it were removed and shown about, the rest was smelted. There was nothing within the "roll" - no bones nor any other object…..The skull was surrounded by softer stuff. There was something like bat bones. There were hard and soft spots in the digging. Next day we looked for the lower jaw, but nothing was found…..Some time afterwards, but in the same day, we found outside of were the bundle was and to one side of it,…… the leg of a man [a tibia, NHM registration number E691]. *There were no other bones...."*.

To summarise: the skull was found in softer sediments, under "*very pure, not very solid lead ore that lay between the crevice or cave that contained the skull and the bulk of the cavity which was filled with more or less mineralized animal bones, detritus etc*" (personal communication of the manager of the mine, Mr. Macartney[36]).

Others who visited the find locality after the discovery of the skull have claimed that numerous other bones were found with it. Bather[37] concluded that an entire human skeleton was probably associated with the skull, but was discarded because its importance had not been recognised.

At this point, a letter from Franklin White to Smith Woodward[38] recently rediscovered in the NHM archives needs mentioning. "*Herewith a diagram of the Rhodesia No 1 – Koppje showing the general outline and position of the Bone Cave where the skull … was found. I have drawn it from my own measurements made in 1907 – 8 and from data given me by Mr. Ross K. Macartney which refers to work done since that time. I hope it will be of use to you. It does not agree with sketches which I have seen published, but I can't help that.*" Extended Data Figure 3 is redrawn from White's sketch. It shows that the Bone Cave was completely unrelated to the skull, which was found near the bottom of a fissure reaching the surface. The most informative picture relating to the position of the skull was also published by the *Illustrated London News*, but never reproduced in any subsequent papers dealing with Broken Hill discovery (Extended Data Figure 4). The fissure mentioned by White (the "New Cave" in the Hill, see Extended Data Figure 4: coordinates E9 to D11) is clearly visible to the left of the spot where the skull was found (Extended Data Figure 4: circle, D12), but there is no clear sign of the bone cave. Also, Oakley[35] suspected that the skull could have been redeposited during the mining operations. The femur EM793 was found at the base of the crevice[39]: "*On the afternoon following this now famous discovery it seems that Mrs Whittington was lowered on a rope into the cavity opened up at the lower end of the deep cave or sinkhole at the go foot level in the opencast. From the rubble that littered the floor of the cavity she recovered the part of the human femur here described together with a large, well made, stone*

spheroid". It is clear from this description that the skull was found in a different place and that the opening was probably not involved in the dislocation of the skull.

When found, the skull was partly encrusted with mineral matter which was described by Spencer[35]: "*The inside of the skull is lined with a crystalline crust 0.1 mm. thick, which chips off as thin flakes and consists of a granular aggregate of minute crystals of hemimorphite (hydrated zinc silicate).*" Small samples of the cranium as well as other human and animal bones from the cave were semi-quantitatively analysed for Pb, Zn and V and it was found that only the skull contained more zinc than lead[35]. This was later confirmed by more quantitative analyses of the human bones[40]. Even the small mammal bones from the matrix which filled the skull were lead-dominated. Whilst this did not necessarily mean that the skull came from a different individual than the other human bones, it meant that it had been exposed to a different geochemical environment. The occurrence of the hemimorphite could be interpreted in two ways either the pocket under the lead ore contained a significant amount of zinc ore, or the skull had fallen from a higher level and was filled with lead dominated sediment and small mammal bones[35]. Oakley speculated that this could have happened during mining operations[35]. Because the walls of the upper part of the bone cave above the water level were lined with hemimorphite crystals, it was concluded that it was unlikely that the skull was deposited in a sediment pocket of zinc ore within the lead carbonate ore, but it was more likely that the hemimorphite precipitated inside the skull was an indication "*that the skull of Kabwe (Rhodesian) man may originally have been deposited in the upper cave...* [and] *...was soon transported in the lower cave where it was found*"[40]. In addition, dense accumulations of small mammal bones were found in the upper part of the bone cave and attributed to either owl pellet deposits or flood accumulation of smaller animals[41] (see Extended Data Figure 3)

2. Biostratigraphy - Macromammals. The fossil mammals from Broken Hill were first described by Hopwood[42], then revised[43] and further commented on[44-48]. An older age for the assemblage was suggested, possibly comparable with the Elandsfontein main fauna[44]. However, recent advances in the dating and biogeographic definition of the mid-Quaternary large mammal succession in southern Africa allow a revised view of the age of the Broken Hill faunal assemblage, if taken as a chronologically cohesive sample (which it is probably not, given its sampling history).

The mid-Quaternary faunal succession in southern Africa includes the Cornelian Land Mammal Age (LMA), now dated to between about 1.07 Ma and 600 ka, and the Florisian LMA, dated between about 600 ka and 10 ka[49-53]. The presence of a sabretooth felid and the genus *Theropithecus*, also found in the Elandsfontein Main assemblage[54], may point to a Cornelian LMA.

However, the rest of the taxa are Florisian in character. Of particular importance is the presence of the hartebeest, genus *Alcelaphus*, which suggests a mid- to late Quaternary Florisian age. Hartebeest has an earliest occurrence date in East Africa of about 600 ka[55], and in southern Africa it is always associated with post-Cornelian contexts[52,53,56]. The absence of other typical Florisian wetland and aquatic marker species, such as the lechwe (*Kobus leche*) and a derived form of Bond's springbok (*Antidorcas bondi*), may be due to sampling bias or its geographic position.

The geographic position of Broken Hill falls in an intermediate boundary zone on the edge of the southern African mammalian subregion. At present we do not have a good appreciation of biogeographic variability in the Cornelian LMA and the Florisian LMA faunas in this area. However, given its geographic position, which is currently in the savannah woodland area of Zambia and which is peripheral to the open grasslands of central southern Africa, there is room to argue for a slightly younger age for the Broken Hill fauna by viewing the archaic forms in the Broken Hill assemblage as evolutionary remnant taxa. The open plains of central southern Africa today contain the characteristic southern endemic grassland taxa, which biogeographically distinguish southern Africa from East Africa. The origin of this distinction can be traced back to c. 1.0 Ma. In the sense of being peripheral to the central open grasslands, Zambia may have provided refugia for remnant taxa. This is also suspected to be the explanation for the Elandsfontein sabretooth, since the Cape ecozone has a long history of preserving archaic forms that had gone extinct elsewhere in Africa. Thus, the Broken Hill mammal fauna probably postdates the end-Cornelian at about 600 ka, even though it may contain archaic-looking survivors of earlier periods, reflecting geographic differences in the expression of the early Florisian LMA within the southern African mammal subregion.

3. Biostratigraphy - Micromammals. The Plio-Pleistocene rodents of East and Southern Africa belong to two distinct biogeographical regions since the lower Pliocene[57]. While the earlier periods have been well documented, very few of the rodents from upper Pleistocene sites have been described. Furthermore the faunas situated between the two regions, such as those from Kabwe, are not yet fully known for their small mammals.

Rodents were abundant at Broken Hill[36] and although faunal lists were published early on[41,42,58], modern taxonomic and taphonomic analyses were only carried out in the early 2000s[59,60]. The micromammals from Kabwe were collected at the time of the discovery of the hominin skull, but the precise origin of many of them (within or outside the cranium) is not always recorded. Barn owl was apparently the main predator of the assemblage[59]. Here, we provide an updated list of the small

436 mammal taxa from Broken Hill, indicating a quite modern fauna of rodents and shrews accumulated
437 by the kind of nocturnal predators living in the Zambezian savannah woodland environment today.
438 In Avery's view, these were deposited during what she termed an interglacial period[60].
439
440 CD examined the rodents that come from sediment within the skull as well as from bulk sediment
441 surrounding the skull, and we have been able to establish biostratigraphic relationships for some
442 taxa to refine the biostratigraphic analyses. The rodents are listed in Supplementary Data Table 1.
443 Thanks to common genera living in both the Zambezian and Somali Masai savannahs, we can
444 compare species affinities.
445
446 The laminate tooth rat *Otomys* has a South African origin and is known to have dispersed after 2.4
447 Ma to the North, arriving in Tanzania at around 1.8 Ma and in Ethiopia at around 0.6 Ma[57,61]. At
448 Broken Hill, the specimens were attributed to the modern *O. angoniensis*[60]. The Broken Hill
449 specimens display an upper M3/ with 6-7 laminae, most of the molars having 6 laminae (5 laminae
450 plus a small cusp at the back of the tooth), but one specimen has 8 laminae. Frequently, there is a
451 trace of cusps on the laminae (Extended Data Figures 6A, B). Their size is intermediate between the
452 fossil *O. petteri* from Olduvai Bed I, *O. gracilis* of Swartkrans and Sterkfontein and the modern *O.*
453 *angoniensis* (Extended Data Figure 7A). They are larger than *Otomys* sp. specimens from Olduvai
454 Bed IV specimens. They display 10 to 11 roots on the M^3. The M_1 has 4 laminae and the incisors
455 have one and a half grooves. They differ from modern *O. angoniensis* by a higher number of roots
456 (only 9-10 roots seen in *O. petteri*), a smaller size, and the fact that the average number of laminae
457 is 7 here, instead of 6. Their morphology places the Broken Hill *Otomys* close to the Kapthurin BK
458 specimens whose associated Ar/Ar age is between 0.6-0.3 Ma[62]. Both share 10 to 11 roots to the
459 upper M3/, and 6 to 7 laminae but the Broken Hill M3/3 are slightly larger than in Kapthurin BK
460 and fit among the smallest specimens of the modern *O. angoniensis* lineage. The Broken Hill
461 *Otomys* retained several primitive characters that agree with an age slightly earlier than 0.3 Ma.
462
463 Remains of the pouched mouse *Saccostomus campestris* were found at Broken Hill, Mumbwa and
464 Twin Rivers[60]. It is represented by one right mandible with three worn lower molars associated with
465 the human cranium and two other specimens of unknown provenance (M12932 cave deposits,
466 Extended Data Figures 6C, D). The first lobe of the M_1 has one large and oblique cusp compared to
467 modern *S. campestris* specimens. The upper and lower M1 from Broken Hill are slightly smaller
468 than (but within the size range of) modern South African, *S. campestris* (Extended Data Figure 7B)
469 and the East African Olduvai Bed IV specimens. If we assume a lineage trend towards a size

reduction in the genus[63], the Broken Hill specimens may be younger or at least of the same age as Olduvai Bed IV (ca 0.8-0.6 Ma).

Among the other rodents, the site also yielded a very large *Arvicanthis* attributed to *A. niloticus*[59,60] but larger than modern representatives of this genus, except for *A. blicki* from Ethiopia. Two species now attributed to *Gerbilliscus* were identified under the names *G. validus* and *G. leucogaster*[59]. They are very modern in size and morphology. The Acacia rat *Thallomys* is widespread in East and Southern Africa today and occurred in various Plio-Pleistocene sites. The Broken Hill specimens were attributed to the South African species *T. paedulcus*[59]. These specimens have the same size as modern representatives of the species but display relatively low stephanodonty. Cusps of the prelobe are less bunodont than in the modern representatives of *T. paedulcus* and similar to *T. quadrilobatus* from Olduvai Bed I. There is a strong labial cingular margin in Broken Hill and a tmA which are generally considered as primitive characters.

Another very abundant rodent, the multimammate rat of the genus *Mastomys*, is found in East and South Africa and two cryptic species are well represented today in Zambia: *M. natalensis* and *M. coucha*. For the upper M1/, the Broken Hill specimens are larger than modern *M. coucha* and *M. natalensis* and reached the same size as modern *M. kollmanspergeri* from central Africa.

The bush rat *Aethomys* was attributed to *A. kaiseri*[59]. Molar morphology and size confirm the Broken Hill *Aethomys* to be closer to modern *A. kaiseri* and *A. selidensis* forms than to the Olduvai and Omo fossil species. The only age information that can be derived from this taxon is that it is more recent than 1.6 Ma.

Other taxa found at Broken Hill like *S. pratensis, L. rosalia, M. musculoides, M. triton and P. fallax* show modern affinities. However, no direct comparisons with fossil material from well dated sites are possible for these species. All these taxa are indicative of southern savannas environment but are also found today in the south of the Somali Masai region[64].

The rodent fauna of Broken Hill clearly belonged to the Zambezian savannah domains and has yielded some of the earliest known representatives of modern species. However, these species clearly kept some archaic characters, and their morphology and size suggest an age between 0.3 and 0.8 Ma. This result fits well with some molecular analyses, which showed that the modern species of *Gerbilliscus* from the southern clade differentiated very early (2.60-3.07 Ma) and the modern *G. brantsii / G. afra* diverged later, between 2.32 and 2.60 Ma[65]. Similarly, the modern *Arvicanthis*

clades diverged in the lower Pleistocene[66]. If the distinction between the Tanzania+Zambian clade from the Southern African was old (3.79-2.55 Ma), the divergence between the Tanzanian and Zambezian clades occurred more recently, between 0.72 and 0.48 Ma[67]. Because we find that *S. campestris* from Olduvai Bed IV and the one from Broken Hill are slightly different, this may indicate that the lineages had already diverged, and that the Broken Hill rodents are younger than the 0.72 -0.48 Ma time range interval.

4. Elemental analysis

Elemental analyses were carried out at the ANU's Environmental Geochemistry laboratory using the laser ablation system coupled with a Varian-820 quadrupole ICP-MS, using NIST 610 glass standards. Oakley[35] had analysed the skull and micro-faunal bones for Pb, Zn and V and observed that only the skull had more Zn than Pb while the opposite applied to all other faunal elements. He concluded that the skull came from a different, unique burial environment. Oakley used small scrapings from the nasal cavity and there was a suspicion that the samples contained significant amount of the hemimorphite crust. We analysed a small dentine fragment from the skull and several small mammal bones (Extended Data Table 2). While the concentrations of Pb, Zn and V are slightly lower in the dentine than the micro-mammal bones, which may simply be a function of different porosities in the different materials, the relative Pb and Zn signatures are very similar. Thus, based on the elemental analysis, we cannot ascertain different burial environments for the small mammals and the skull. Perhaps the much higher vanadium concentrations in the small mammals may support a separate burial environment, but the V concentrations seem highly variable (average: 373±552 ppm).

The elemental analyses of the sediment samples in Extended Data Table 11 were carried out using the commercial service of Genalysis, Perth, using total solution ICP-MS.

5. U-series analysis

Laser ablation analyses were carried out at the ANU's Environmental Geochemistry laboratory. This system was described in detail[68]. A Neptune multi-collector ICP-MS was used for the measurements of U-concentrations and U-series isotopes. TIMS U-series dating was carried out at different laboratories. The calcitic crust (hide) was analysed in 1994, using routine methods[69]. Samples from the cross section of the femoral midshaft were analysed in 2006 at the Open University[70], small surface samples of the other two bone fragments and the dentine at ANU[71], a micro-mammal bone at the University of Queensland[72]. The gamma spectrometric data were obtained with the system and methodology used at ANU[73].

5.1. U-series results

The U-series results of the human remains are shown in Figure 2A and Extended Data Tables 3 to 9. The results of the small mammals found inside and surrounding the skull (Extended Data Tables 3, 10), as well as the calcitic layer found in the vicinity of the skull ("hide"; Extended Data Table 3), are shown in Figure 2B. All isotope ratios are activity ratios with 2σ errors, as are the errors of the cited age estimates. Before discussing the individual results, one must keep in mind that most U-series results on bones have to be regarded as minimum age estimates because uranium is taken up post-mortem. Thus, the calculated closed system U-series ages must be regarded as minimum apparent ages.

5.1.1. Skull (E686)

Three domains of the skull were analysed for U-series isotopes. Firstly, the dentine attached to the tooth enamel fragments that were used for ESR (see below), was analysed by thermal ionisation mass spectrometry (TIMS, see Extended Data Table 3). Secondly, two domains of a detachable basioccipital fragment were analysed by laser ablation ICP-MS, the volumes close to the inner and outer surfaces. To minimise any damage, the laser was used to drill a series of holes[74] into the fragment from both bone surfaces (for the locations see Extended Data Figure 9). The fragment was measured in 2014 and 2016. It turned out that the Broken Hill samples had extremely high concentrations of heavy elements causing a very large number of heavy low energy ions to enter the mass spectrometer. The cup configuration for U-series measurements of the Neptune mass spectrometer at ANU is shown in Table 1 of[68]. ^{234}U is measured by a central SEM while ^{230}Th is measured by a compact discrete dynode (CDD) electron multiplier. The central SEM is set back from the faraday cup plane and is well guarded from low energy ions. The CDD, however, is in the plane of the faraday cups and is less well shielded from low energy ions. This caused very high background signals in the 2014 ^{230}Th measurements, which was not immediately recognised because background and tailing measurements were carried out on the rhino standard, which has no contaminations with heavy elements. By the time this problem was addressed, the sample had been returned to the Natural History Museum. In 2016, the fragment was re-measured by using the central SEM for ^{230}Th. As the result we have two independent data sets for $^{230}Th/^{238}U$ and $^{234}U/^{238}U$.

The detailed analytical data of the basioccipital fragment are given in the Extended Data Tables 4 and 5. For the calculation of depth dependent apparent U-series ages, the $^{234}U/^{238}U$ and $^{230}Th/^{238}U$ data streams were averaged (Extended Data Table 6; the $^{230}Th/^{238}U$ data of the outside hole #1 were not used as it showed anomalously low U-concentrations, see Extended Data Table 4). It is interesting to note that the holes drilled from the outside surface into the basioccipital fragment

have generally both higher $^{234}U/^{238}U$ and $^{230}Th/^{238}U$ ratios than the holes drilled from the inside (Extended Data Figures 10A, B). The $^{230}Th/^{238}U$ ratios indicate some secondary overprint in the first three data points of the averaged inside holes as well as the last four of both sets (Extended Data Figure 10C). There is some scatter in the individual age estimates (Extended Data Table 6, Extended Data Figure 10C), but apart from the first three data points, the errors overlap. There may be some structure in the age-depth profile for data points 4 to 26, but the uncertainties prevent any detailed analysis. Most of the variations are likely due to uranium micro-migration[75]. The best age estimate is derived from the averaged isotope values from data point 4 to 26, which is 298±34 ka for the inside holes and 301±37 ka for the outside holes. The weighted mean of 299±25 ka is the best estimate for the U-uptake event of the basioccipital fragment. This result is 83±25 ka older than the result of the dentine. However, when calculating the initial $^{234}U/^{238}U$ activity ratios, the dentine and fragment ratios agree within error (7.419±0.064 vs 7.122±0.475 and 7.696±0.557). This indicates that the U-source for both skeletal elements had remained the same, but also that the U-source for the skull is distinctively different to all other materials from Broken Hill that were analysed with U-series (see Figure 2). The question is whether the age differences between the dentine and the basioccipital fragment are due either to leaching of uranium from the bone or to delayed U-accumulation in the dentine. If the bone had the same U-history as the dentine, followed by leaching, the bone samples would more or less have the same measured $^{234}U/^{238}U$ ratios as the dentine, i.e. their data would lie to right of the dentine in Figure 2A. This would result in significantly higher initial $^{234}U/^{238}U$ ratios. Instead, the basioccipital results lie (within error) on the same $^{234}U/^{238}U$ isotope evolution line as the dentine, indicating that the source of the uranium had remained the same (see above). Therefore, time lapse between the basioccipital fragment and the dentine is most likely the due to a delayed start of the U-uptake into the dentine, or that the dentine stayed an open system for longer. We therefore regard the basioccipital results to be better representations for the minimum age estimates of the skull.

5.1.2. Femur midshaft (EM793)

The femoral midshaft (EM793, Extended Data Figure 5C) was analysed with three different U-series analyses. Extended Data Figure 8 shows the comparison of laser ablation, TIMS and gamma spectrometry. Laser ablation sampled a surface layer of less than 20 μm, samples for TIMS were drilled to a depth of few mm and gamma spectrometry measures the bone as a whole. For comparison, all U-series isotopic ratios are given as activity ratios. Because of the low kinetic energy of the emissions of ^{234}Th (63.3 keV) and ^{230}Th (67.7 keV), gamma spectrometric $^{230}Th/^{238}U$ ratios are dominated by the surface layers facing the detectors. The $^{234}U/^{238}U$ activity ratios of TIMS and laser ablation are indistinguishable. Gamma spectrometric $^{234}U/^{238}U$ ratios are not shown

as they are associated with extremely large errors due to the small probabilities of gamma emissions from ^{234}U combined with interferences from other U-series isotopes[73]. The average $^{230}Th/^{238}U$ ratios of TIMS (2.4812±0.0495, Extended Data Table 3) and laser ablation (2.555±0.066, Extended Data Table 7) agree well within the 2σ error range. The high resolution laser ablation results, however, imply far more complex U-migration patterns than the TIMS analyses. The gamma spectrometric $^{230}Th/^{234}U$ ratio of 2.722±0.061 overlaps with the laser ablation data but is slightly higher than the TIMS result. This may be because the gamma spectrometric measurements derive from different volumes than the other two methods. The gamma spectrometric $^{231}Pa/^{235}U$ ratio is close to equilibrium, which implies that little overall U-mobilisation has taken place over the last 130 ka. If at all, the Pa/U ratios suggest that a small amount of leaching may have occurred. The initial $^{234}U/^{238}U$ ratio of the average TIMS result is 3.963±0.052. We can conclude that the three different measurement approaches for U-series data provided comparable results, indicating a U-series uptake event during MIS 6.

5.1.3 Proximal Femur (E907)

The femur head was analysed by TIMS and gamma spectrometry (Extended Data Tables 3 and 8). Both yielded ages of around 160 ka. The initial $^{234}U/^{238}U$ ratio derived from the TIMS analysis is 4.034±0.006. The two femur fragments (EM793 and E907) yielded comparable U-series results, indicating that both were deposited in a closely similar geochemical burial environment, although they come from different bones[39].

5.1.4. Os Coxa (E719)

The os coxa yielded a surprisingly young TIMS Th/U age of 117.1±0.5 ka (Extended Data Table 3). However, this analysis was carried out on a very small surface fragment. Several other samples also showed a secondary overprint (see Extended Data Figures 8 and 10B, C). The whole bone yielded an older gamma spectrometric age of 165±9 ka with compatible $^{231}Pa/^{235}U$ results (Extended Data Table 8). This indicates a U-uptake event during MIS 6.

5.1.5. Tibia (E691)

The tibia was analysed using with laser ablation along with the basioccipital fragment of the skull, and thus the same analytical procedures apply. The results are shown in Extended Data Table 9. Spot analyses were carried out along two transects. There are no trends in transect 1 while the first two spot analyses of transect 2 show some secondary overprint. The remaining data from transect 2 are indistinguishable from transect one, both implying a U-uptake event during an early phase of MIS 6 at around 180 ka ago. The initial $^{234}U/^{238}U$ ratio derived from the two transects is 5.897±0.120.

5.1.6. Small mammal bones found in the sediment in and around the skull.

The small mammal bones present the only datable material that was found in physical context with the skull. Four samples from the sediment inside the skull were analysed in 2010, using discrete sampling spots, while in 2016, the laser was used to drill deeper holes[74]. The analyses are summarised in Extended Data Table 10 and Figure 2B. The 2016 analyses were carried out on bones that were described in the microfauna section. As it can be seen in Figure 2B, there are no obvious differences between the results from the small mammals found inside and outside the skull. The data seem to fall into two distinctive clusters, one having an average age around 136 ka, the other around 108 ka. Their initial $^{234}U/^{238}U$ ratio is closely similar with 3.958±0.062 and 3.967±0.071, for clusters 1 and 2, respectively. This indicates that the source of the uranium was the same and that perhaps two faunal deposition events may be present. The earlier U-uptake took place during the transition of MIS 6 to MIS 5 while the younger event took place during MIS 5 (i.e. 71 - 130 ka).

5.1.7. Calcitic Layer ("hide")

Two TIMS analyses of the calcitic layer yielded age of 137.6±1.4 and 175±0.2 ka. The calcitic layer was formed on a surface of a clastic sediment during MIS 6.

6. ESR analysis

ESR analysis was carried out on three small tooth enamel fragments from a molar of skull E686. These measurements and dose evaluation were described in great detail[76,77]. It was concluded that the dose derived from the stable of CO_2^- radicals was 774±13 Gy.

The skull influences the dose rate to the tooth in two ways: on the one hand, part of the sediment dose rate is shielded, on the other hand the uranium in the skull provides gamma dosage to the tooth. We have simulated the effect for the Broken Hill skull[78], using the data provided in Extended Data Table 12, and found that the skull shields the tooth for 7.64% of the external gamma dose rate from U, 6.9% from Th and 6.3% from K. The external sediment U, Th, and K gamma dose rates were reduced accordingly.

For the calculation of the gamma dose rate from the skull, it is convenient to calculate the closed system dose. Using the average U-concentrations of the basioccipital fragment (11.9±0.4 ppm) and the average $^{230}Th/^{238}U$ (4.343±0.043) and $^{234}U/^{238}U$ (3.748±0.036) ratios, a dose of 120±18 Gy is obtained. This is reduced to 93±9 Gy for a water content of 20±10%. In addition, the skull was CT scanned on at least three separate occasions, plus a small but unknown number of X-rays were

taken in its early history We conservatively estimate that these procedures produced an equivalent dose of around 60±20 Gy in the tooth enamel[79]. For the ESR age calculations, the measured dose was reduced to 621±26 Gy. We did not obtain U-series isotope data for the enamel - we assumed them to be the same as for the dentine.

The main problem of any ESR dating attempt is the difficulty in reconstructing the environmental dose rates to the tooth enamel. The only material that was directly related to the skull, is the sediment that was removed from it. After several years of trying to find original material in the Natural History Museum, two small vials were found that clearly state that they contained material that was scraped off the original skull in 1921 (see Extended Data Figure 11). In the first instance one can assume that this sediment provided most of the external dose rate to the skull. The small mammal bones could perhaps have been incorporated into the sediment at a later stage. As it cannot be excluded that the association between the skull and the sediment occurred at a later stage in the burial history of the skull, we collected another 20 lose sediment, breccia and rock samples from the site to randomly generate environmental beta and gamma dose rate distributions. We used four models, which all had the basic assumption that the skull was located in an open cavity and was itself not filled with sediment. There are two gamma sources: the roof of the cavity and the underlying cavity floor. A random number generator was used to firstly select a component of the gamma source and secondly to determine its percentage. Material was added until the composition reached >95%, the rest was filled by another randomly selected material. The beta dose rate was derived from a single randomly selected source material. In all models, the roof of the cavity is composed of solid materials (rocks, #15-20 in Extended Data Table 11, and breccia, #7 to 14). Each model ran for 10,000 dose rate calculations. For the cavity floor, Model 1 assumes that it is composed of any material in Extended Data Table 11. In Model 2, the cavity floor is composed of loose sediment and breccia (E686 and #1 to 14), in Model 3 of lose sediment (E686 and #1 to 7) and in Model 4 of sediment E686 only.

Extended Data Figure 12 shows the dose distributions of the four models. The dose distributions are clearly heavily skewed. In order to obtain numerical values for further calculations, the lower end of the dose rate distribution was treated as a normal distribution. The mean value was obtained at the 50% level and the pseudo 2-σ range from the 6.68% level (equivalent to a normal distribution). Mean values and the pseudo 2σ ranges are shown in Extended Data Table 13.

In order to use these dose distributions for assessing maximum possible ESR ages, internal closed system alpha and beta doses were calculated similar to external gamma dose from the skull[80]. The

combined alpha and beta doses are 442±47 Gy, which results in an external dose component of 179±77 Gy. This dose is the component that can be generated from sources external to the skull.

6.1. ESR results

Using the values in Extended Data Table 12 for the calculation of a combined U-series/ESR age estimation[81] with the ESR DATA program[82], an age of 256+66/-52 ka is obtained (2-σ errors).

The dose rate distributions can be used to calculate maximum possible ages by dividing the external dose of 166±75 Gy by the mean model dose and using the combined 2-σ errors to define a maximum age (these are listed in Extended Data Table 13).

6.2. Discussion

It must be clearly stated that it is not possible to calculate any meaningful ESR age estimates because we do not know the actual geological environment of the skull. However, ESR can be used to assess possible upper age limits. The straightforward U-series/ESR age calculation, using sediment E686 as the only external beta and gamma source, yields an upper 2-σ age limit of 322 ka. This agrees well with the upper age limit of the U-series analysis of the basioccipital bone (324 ka). The calculated p-value of -0.93 indicates a slightly delayed U-uptake into the dentine and enamel. The corresponding initial $^{234}U/^{238}U$ ratio of 7.680 is well within the range of the apparently older measurement on the basioccipital fragment (Extended Data Table 6). Using any of the other modelled external dose rate distributions will result in younger ages. For models 1 to 3, most calculations will lead to data sets for which no combined U-series/ESR age can be calculated (i.e. the ESR age would be younger than the closed system U-series age).

The maximum ages of the four dose rate distribution models (Extended Data Table 13) must be regarded as extreme cases, as all other parameters were kept to the minimum possible values. Models 1 to 3 all yield ages that are younger than the minimum U-series age obtained on the basioccipital fragment. Only Model 4 would allow ages of up to 312 ka.

The ESR calculations strongly support a scenario where the initial U-accumulation into the skull bone took place shortly after it was buried. The U-series system for the bones of the skull became closed shortly afterwards. The diffusion of uranium into the dentine seem to have continued for a considerable time, which explains the difference between the closed system U-series ages of the dentine and the basioccipital fragment. While we cannot present a firm mathematical calculation for how much older the skull was than the U-series results of the basioccipital fragment, the ESR

754 results strongly imply that its age is most likely within the error envelope of the closed system U-
755 series age of 299±25 ka.
756
757 **References**

758 33. White, F., 1908. Notes on a cave containing fossilized bones of animals, worked pieces of bone,
759 stone implements, and quartzite pebbles, found in a kopje or small hill composed of zinc and
760 lead ores, at Broken Hill, North-Western Rhodesia. *Proceedings of the Rhodesian Scientific*
761 *Association* 7:13-21.
762 34. Harris, W.E., 1921. The finding of the Broken Hill skull: The mystery of the Great Bone Cave.
763 *The London Illustrated News,* Nov 19th 1921, 679-681.
764 35. Clark, J.D., Oakley, K.P., Wells, L.H., McClelland, J.A., 1947. New studies on Rhodesian Man.
765 Journal of the Royal Anthropological Institute 77, 7-32.
766 36. Hrdlička, A, 1930. The skeletal remains of early man. Washington: *Smithsonian Institution*
767 *Miscellaneous Collections* volume 83.
768 37. Pycraft, W.P., Smith, G.E., Yearsley, M., Carter, J.T., Smith, R.A., Hopwood, A.T., Bate,
769 D.M.A., Swinton, W.E., 1928. *Rhodesian Man and Associated Remains*. London: British
770 Museum (Natural History).
771 38. White, F., 1921. Letter to Smith Woodward (dated 20th November 1921). NHM Archives
772 39. Clark, J.D., Brothwell, D.R., Powers, R., Oakley, K.P. 1968. Rhodesian man: notes on a new
773 femur fragment. Man 3, 105-111.
774 40. Bartsiokas, A., 1989. Studies of recent and fossil bone, including X-ray microanalysis, with
775 special reference to Kabwe (Rhodesian) Man. Unpublished PhD thesis, Division of
776 Anatomy, University of London, 396 pp.
777 41. Chubb, C.E., 1908. List of vertebrate remains. Proceedings of the Rhodesian Scientific
778 Association 7:21-23.
779 42. Hopwood, A.T., 1928. Mammalia. In: Pycraft, W.P. *et al.* Rhodesian Man and associated
780 remains. *Bull. Brit. Mus. (Nat. Hist.)*, pp. 70-73.
781 43. Leakey, L.S.B. 1959. A Preliminary Re-assessment of the Fossil Fauna from Broken Hill, N.
782 Rhodesia. Appendix in: Clark, J.D. Further Excavations at Broken Hill. *J. R. Anthrop. Inst.*
783 89: 225-231.
784 44. Klein, R.G., 1973. Geological antiquity of Rhodesian Man. *Nature* 244:311-312.
785 45. Churcher, C.S. 1978. *Giraffidae*. In Maglio, V.J. and Cooke, H.B.S. (eds.) *Evolution of African*
786 *Mammals*. Harvard University Press, Cambridge, pp. 509-535.
787 46. Churcher, C.S., Richardson, M.L., 1978. *Equidae*. In Maglio, V.J. and Cooke, H.B.S. (eds.)
788 *Evolution of African Mammals*. Harvard University Press, Cambridge, pp. 379-422.

789 47. Gentry, A.W., 1978. *Bovidae*. In V.J. and Cooke, H.B.S. (eds.) *Evolution of African Mammals*.
790 Harvard University Press, Cambridge, pp. 540-572.
791 48. Savage, R.J.G. 1978a. *Equidae*. In Maglio, V.J. and Cooke, H.B.S. (eds.) *Evolution of African*
792 *Mammals*. Harvard University Press, Cambridge, pp.249-267
793 49. Grün, R., Brink, J.S., Spooner, N.A., Taylor, L., Stringer, C.B., Franciscus, R.G., Murray, A.S.,
794 1996. Direct dating of Florisbad hominid. *Nature* 382: 500-501.
795 50. Lacruz, R., Brink, J.S., Hancox, P.J., Skinner, A.R., Herries, A., Schmid, P., Berger, L.R., 2002.
796 Palaeontology and geological context of a Middle Pleistocene faunal assemblage from the
797 Gladysvale Cave, South Africa. *Palaeontologia Africana* 38: 99-114.
798 51. Brink, J.S., 2005. The evolution of the black wildebeest (*Connochaetes gnou*) and modern large
799 mammal faunas of central southern Africa. D.Phil. dissertation, University of Stellenbosch.
800 52. Brink, J.S., Herries, A.I.R., Moggi-Cecchi, J., Gowlett, J.A.J., Bousman, B., Hancox, J.P., Grün,
801 R., Eisenmann, V., Adams, J.W., Rossouw, L., 2012. First hominine remains from a ~1.0
802 million year old bone bed at Cornelia-Uitzoek, Free State Province, South Africa. Journal of
803 Human Evolution 63: 527-535.
804 53. Brink, J.S., 2016. Faunal evidence for mid- and late Quaternary environmental change in
805 southern Africa. In: Knight, J. and Grab, S.W. (eds) Quaternary environmental change in
806 southern Africa: physical and human dimensions. pp 284-305. Cambridge University Press.
807 54. Klein, R.G., Avery, G., Cruz-Uribe, K., Steele, T., 2007. Mammalian fauna associated with an
808 archaic hominin skullcap and later Acheulean artifacts at Elandsfontein, Western Cape
809 Province, South Africa. *Journal of Human Evolution* 52: 164 – 186.
810 55. Vrba, E.S., 1997. New fossils of Alcelaphini and Caprinae (Bovidae, Mammalia) from Awash,
811 Ethiopia, and phylogenetic analysis of Alcelaphini. *Palaeontologia Africana* 34: 127-198.
812 56. Klein, R.G., 1984. The large mammals of southern Africa: late Pliocene to recent. In R.G. Klein
813 (ed.), *Southern African prehistory and palaeoenvironments*. A.A. Balkema, Rotterdam, pp.
814 107-146
815 57. Denys, C., 1999. Of mice and men. Evolution in East and South Africa during Plio-Pleistocene
816 times. In *African Biogeography, Climate Change and Human Evolution*. ed. T. Bromage
817 and F. Schrenk. Oxford: Oxford University press, pp. 226-252.
818 58. Mennell, F.P., Chubb, E.C., 1907. On an African occurrence of fossil Mammalia associated
819 with stone implements. *Geological Magazine* 4: 443-448.
820 59. Avery, D.M., 2002. Taphonomy of micromammals from cave deposits at Kabwe (Broken Hill)
821 and Twin Rivers in central Zambia. Journal of Archaeological Science 29, 537-544.

822 60. Avery D.M., 2003. Early and middle Pleistocene environments and hominid biogeography;
823 micromammalian evidence from Kabwe, Twin Rivers and Mumbwa Caves in central
824 Zambia. Palaeogeography, Palaeoclimatology, Palaeoecology 189, 55669
825 61. Denys, C., 2003. Evolution du genre *Otomys* (Rodentia, Muridae) au Plio-Pléistocène d'Afrique
826 orientale et austral. In *Advances in Vertebrate Paleontology, "Hen to Panta,"* Volume in
827 Honor of Constantin Radulescu and Petre Mihai Samson, ed. A. Petrulescu and E. Stiuca.
828 Bucharest, Romania: Romanian Academy, "Emil Racovitzã," Institute of Speleology, pp.
829 75-84
830 62. Deino A.L., McBrearty, S., 2002. ^{40}Ar/^{39}Ar dating of the Kapthurin Formation, Baringo,
831 Kenya. *Journal of Human Evolution* 42, 185–210.
832 63. Denys, C., Jaeger, J.J., 1986. A biostratigraphic problem: the case of the East African Plio-
833 Pleistocene rodent faunas. *Modern Geology,* 10, 215-233.
834 64. Monadjem, A., Taylor, P.J., Denys, C., Cotteril, F., 2015. *Rodents of Sub-Saharan Africa. A*
835 *biogeographic and taxonomic synthesis.* Walter de Gruyter (ISBN 978-3-11-30166-3), pp.1-
836 1092.
837 65. Colangelo, P., Granjon, L., Taylor, P.J., Corti, M., 2007. Evolutionary systematics in African
838 gerbilline rodents of the genus *Gerbilliscus*: inference from mitochondrial genes. *Mol.*
839 *Phylogenet. Evol.* 42, 797-806.
840 66. Dobigny, G., Tatard, C., Gauthier, P., Ba, K., Duplantier, J.M,, Granjon, L., Kergoat, G.J.,
841 2013. Mitochondrial and nuclear genes-based phylogeography of *Arvicanthis niloticus*
842 (Murinae) and Sub-Saharan open habitats Pleistocene history. *PLoS ONE* 8(12): DOI:
843 10.1371/journal.pone.0077815.
844 67. Corti M., Castiglia R., Annesi F., Verheyen, W. 2004. Mitochondrial sequences and karyotypes
845 reveal hidden diversity in African pouched mice (subfamily Cricetomyinae, genus
846 *Saccostomus*). *J. Zool., Lond*. 262, 1–12.
847 68. Grün, R., Eggins, S., Kinsley, L., Mosely, H., Sambridge, M., 2014. Laser ablation U-series
848 analysis of fossil bones and teeth. Palaeogeography, Palaeoclimatology, Palaeoecology 416,
849 150-167.
850 69. McDermott, F., Stringer, C., Grün, R., Williams, C.T., Din, V.K., Hawkesworth, C.J., 1996.
851 New Late-Pleistocene Uranium-Thorium and ESR dates for the Singa hominid (Sudan).
852 Journal of Human Evolution 31: 507-516.
853 70. Pike, A.W.G., Hedges, R.E.M., Van Calsteren, P., 2002. U-series dating of bone using the
854 diffusion-adsorption model. Geochimica et Cosmochimica Acta 66, 4273-4286.

71. Grün, R., Yan, G., McCulloch, M., Mortimer, G., 1999. Detailed mass spectrometric U-series analyses of two teeth from the archaeological site of Pech de l'Aze II: implications for uranium migration and dating. Journal of Archaeological Science 26, 1301-1310.

72. Price, G.J., Feng, Y.X., Zhao, J.X., Webb, G.E., 2013. Direct U-Th dating of vertebrate fossils with minimum sampling destruction and application to museum specimens. Quaternary Geochronology 18, 1-8.

73. Simpson, J.J., Grün, R., 1998. Non-destructive gamma spectrometric U-series dating. Quaternary Science Reviews 17: 1009-1022.

74. Benson, A., Kinsley, L., Defleur, A., Kokkonen, H., Mussi, M., Grün, R., 2013. Laser ablation depth profiling of U-series and Sr isotopes in human fossils. Journal of Archaeological Science. 40: 2991-3000.

75. Duval, M., Aubert, M., Hellstrom, J., Grün, R., 2011. High resolution, LA-ICP-MS mapping of U and Th isotopes in an Early Pleistocene equid tooth from Fuente Nueva-3 (Orce, Andalusia, Spain). Quaternary Geochronology 6, 458-467.

76. Grün, R., Joannes-Boyau, R., Stringer, C., 2008. Two types of CO_2^- radicals threaten the fundamentals of ESR dating of tooth enamel. Quaternary Geochronology 3: 150-172.

77. Joannes-Boyau, R., Grün, R., 2011. A comprehensive model for CO_2^- radicals in fossil tooth enamel: implications for ESR dating. Quaternary Geochronology 6, 82-97.

78. Nathan, R., Grün, R., 2003. Gamma dosing and shielding of a human tooth by a mandible and skull cap. Ancient TL 21: 79-84.

79. Duval, M., Martín-Frances, L., 2017. Quantifying the impact of μCT-scanning of human fossil teeth on ESR age results. American Journal of Physical Anthropology 163, 205-212.

80. Grün, R., 2000. An alternative for model for open system U-series/ESR age calculations: (closed system U-series)-ESR, CSUS-ESR. Ancient TL 18, 1-4.

81. Grün, R., Schwarcz, H.P., Chadam, J.M., 1988. ESR dating of tooth enamel: Coupled correction for U-uptake and U-series disequilibrium. Nuclear Tracks and Radiation Measurements 14, 237-241.

82. Grün, R., 2009. The DATA program for the calculation of ESR age estimates on tooth enamel. Quaternary Geochronology 4: 231-232.

83. The London Illustrated News, Nov 19th 1921, page 681.

Acknowledgement

Aspects of this research were funded by ARC grants DP0664144 (Grün et al.) *Microanalysis of human fossils: new insights into age, diet and migration*, DP0666084 (Roberts et al) *Out of Africa and into Australia: robust chronologies for turning points in modern human evolution and*

dispersal, DP110101415 (Grün et al.) *Understanding the migrations of prehistoric populations through direct dating and isotopic tracking of their mobility patterns.* Chris Stringer would like to acknowledge support from the Calleva Foundation and the Human Origins Research Fund, as well as the valuable assistance of past and present members of staff at the Natural History Museum Robert Kruszynski, Laura Buck, Gillian Comerford, Lorraine Cornish, Chris Collins, Linzi Harvey, Julia Galway-Witham and Pip Brewer.

Author Contributions

RG and CS wrote the paper with contributions from all co-authors. RG carried out the ESR measurements, RJB ESR spectrum deconvolution. Laser ablation analyses was done by RG and AP, with the support of SE and LK; U-series solution analyses by GM, FMcD, TC; gamma spectrometric measurements by RG; U-analysis of tooth enamel by MA; micro-faunal analysis by CD; macro-faunal analysis by JB. MR provided the site history and tracked down some of the sediment samples.

Extended Data Figure Captions

Figure 1: Photos of the skull shortly after its discovery[36].A: The cranium at the place where it was found; B: with Tom Zwigelaar who discovered the skull, C: frontal and D lateral view before the matrix was removed.

Figure 2: Drawing of the bone Cave[34]

Figure 3: Drawing of the Bone Cave after White[38]

Figure 4: Photo of the site with finding spot of the skull[83].

Figure 5: Other Broken Hill human fossils sampled for direct dating. A. Partial os coxa (E719); B. Femoral fragment (E907); C. Femoral midshaft (EM793); D. Tibia (E691).

Figure 6: A: SEM picture of Broken Hill *Otomys angoniensis* mandible fragments with lower M/12

B SEM picture of Broken Hill *Otomys angoniensis* upper M3/ (7 laminae)

Drawing of the lower (C) and upper (D) first molars of *Saccostomus campestris* from the cave deposits

Figure 7: A: Fossils and modern Otomys upper M3 scatterplot of length versus width in mm. Abbreviations : SE Sterkfontein Extension, Bed I, Bed II, Bed IV : Olduvai Bed II and Bed IV, KB : Kromdraai B, BH : Broken Hill. Modern specimens of O.angoniensis and O. saundersae have been added for comparison.

B: Scatterplot (length x width in mm) of the modern and fossil *Saccostomus* species upper first molar . *Saccostomus major* is a Pliocene species found in Laetoli (3.7-2.5 Ma) ; *S*.cf. *mearnsi* was described in Olduvai Bed I (1.7-1.6 Ma), Bed IV: *Saccostomus* cf. *campestris* from Olduvai Bed IV (0.8 Ma), *Saccostomus* sp. from East Turkana (1.6 Ma), *Saccostomus campestris* from Broken Hill. The modern *S.mearnsi* live in East Africa and the modern *S.campestris* live in South Africa. The correlation lines are indicated here.

Figure 8: U-series results by laser ablation, solution ICP-MS and gamma spectrometry on the femoral midshaft (EM793). All data points are averages from the isotopic measurements with 2 standard deviation errors. The laser ablation profiles consists of (n=33, Extended Data Table 7) and the TIMS of (n=5, Extended Data Table 3) measurements across the bone. The gamma spectrometry is carried out on the whole sample (n=1, Extended data Table 8).

Figure 9. Laser sampling positions on the basioccipital fragment. Red: 2014 $^{234}U/^{238}U$ measurements, green: 2016 $^{230}Th/^{238}U$ measurements. A: outer surface, B: inner surface.

Figure 10:

Figure 11: Vials with sediment scraped off the skull (sediment E686 in Supplementary Data Table 11).

Figure 12: External dose rate distributions for different models using the materials listed in Extended Data Table 11. In all models the cave roof is composed of solid material (rocks and breccia). A: floor is composed of any material in; B: the cave floor is composed of loose sediment and breccia; C: the cave floor is composed of loose sediment, D: the floor only consists of sediment E686. E: sorted dose rates for the lower 50% of results.

Extended Data

Extended Data Table 1: Faunal list of Broken Hill small mammals

Species	Within the skull	Bulk sediment
Saccostomus campestris	1	2
Steatomys pratensis	2	x
Gerbilliscus validus	6	x
Gerbilliscus leucogaster	x	1
Aethomys kaiseri	19	
Aethomys chrysophilus	x	x
Arvicanthis sp.	3	20
Lemniscomys rosalia	x	x
Mastomys sp.	44	x
Mus minutoides	3	X
Mus triton	14	X
Pelomys fallax	34	X
Grammomys dolichurus	7	
Thallomys paedulcus	10	X
Otomys angoniensis	53	3
Cryptomys hottentotus	1	
Elephantulus brachyrhynchus	?	X
Crocidura fuscomurina	?	x
Crocidura hirta	?	X
Crocidura luna	?	X
Crocidura mariquensis	?	X
Crocidura turba	?	X
Suncus varilla	?	x

Extended Data Table 2: Elemental analyses on skull E686 and rodent material found inside the skull

Semi-quantitative analyses, Oakley (1947)				Laser ablation (ppm)			
	Pb	Zn	V		Pb	Zn	V
BH Skull	4	15	trace	BH-A	44.8	15.2	28
				BH-B	30.9	14.1	16
Rodent	20	5	0.3	Rodent-1A	49.9	19.0	103
				Rodent-1B	47.2	17.9	96
				Rodent-2A	44.6	18.4	49
				Rodent-2B	48.8	15.9	54
				Rodent-3A	64.3	17.2	1448
				Rodent-3B	59.0	19.4	489

Extended Data Table 3: Solution U-series results (Errors: 2 s.d.))

Sample	$^{230}Th/^{238}U$	$^{230}Th/^{238}U$ error	$^{234}U/^{238}U$	$^{234}U/^{238}U$ error	$^{230}Th/^{232}Th$	Age (ka)	Age error (ka)	Initial $^{234}U/^{238}U$	$^{234}U/^{238}Ui$ error
[1]Skull (E686)									
Dentine	4.6234	0.0334	4.4914	0.0170	>10000	215.8	4.0	7.4188	0.0644
[2]Femur Midshaft (EM793)									
A	2.4563	0.0266	2.9648	0.0181	>10000	146.4	3.3	3.9697	0.0270
B	2.5134	0.0267	2.9311	0.0174	>10000	155.9	3.5	3.9984	0.0283
C	2.5195	0.0266	2.8763	0.0199	>10000	162.6	4.0	3.9685	0.0300
D	2.5063	0.0266	2.9341	0.0181	>10000	154.8	3.5	3.9936	0.0282
E	2.4106	0.0260	2.9133	0.0210	2709	146.3	3.4	3.8913	0.0276
Average	2.4812	0.0495	2.9239	0.0346		153.0	6.5	3.9629	0.0523
[1]Femur Head (E907)									
	2.5423	0.0060	2.9418	0.0028	>10000	158.1	0.8	4.0337	0.0062
[1]Pelvis (E719)									
	1.8997	0.0049	2.6322	0.0025	575	117.6	0.5	3.2743	0.0038
[3]Rodent									
2016o-K	2.1198	0.0047	3.1930	0.0026	445	102.2	0.4	3.9258	0.0037
[4]Calcitic Layer (hide)									
1	3.0222	0.0168	3.7394	0.0084	>10000	137.6	1.4	5.0394	0.0159
2	3.2067	0.0014	3.4834	0.0016	>10000	175.1	0.2	5.0711	0.0019

[1] solution TIMS, Australian National University
[2,4] solution TIMS, Open University
[3] solution ICP-MCMS, University of Queensland
[4] solution TIMS, University of Bristol

Extended Data Table 4: 2016 laser ablation $^{230}Th/^{238}U$ runs on basicranial fragment. For hole positions, see Extended Data Figure 8. nd: not detemined, Th concentration below background. Errors are 2 s.d.

	Inside Hole #1					Inside Hole #2				
Bin #	U (ppm)	Th (ppb)	U/Th	$^{230}Th/^{238}U$	$^{230}Th/^{238}U$ error	U (ppm)	Th (ppb)	U/Th	$^{230}Th/^{238}U$	$^{230}Th/^{238}U$ error
1	14.0	12.3	1141	5.210	0.111	14.9	4.4	3360	4.578	0.066
2	12.9	1.6	8150	4.669	0.117	13.0	8.3	1559	4.766	0.072
3	11.9	4.1	2911	4.064	0.067	13.6	8.7	1571	4.990	0.065
4	11.2	8.0	1395	4.147	0.090	11.0	4.5	2440	4.740	0.114
5	10.2	5.7	1771	4.188	0.102	10.0	12.6	798	4.114	0.084
6	10.7	4.7	2296	4.143	0.053	10.3	3.6	2891	4.038	0.070
7	10.6	3.0	3493	4.294	0.052	9.8	6.4	1527	3.996	0.070
8	10.6	2.8	3771	4.538	0.066	10.2	3.8	2684	4.201	0.069
9	9.2	4.4	2074	4.256	0.066	8.2	1.2	6861	4.067	0.071
10	9.2	3.4	2684	4.373	0.057	8.2	1.4	5937	4.174	0.089
11	7.7	5.3	1467	4.426	0.097	7.1	11.9	594	4.133	0.081
12	7.3	1.6	4654	4.441	0.070	6.1	6.6	930	4.019	0.061
13	6.4	2.6	2416	4.446	0.061	5.7	1.3	4432	4.219	0.087
14	5.4	6.4	845	4.356	0.072	5.0	1.2	4183	4.097	0.081
15	5.1	1.2	4259	4.484	0.082	4.3	1.1	4017	4.158	0.092
16	4.8	0.5	9066	4.567	0.088	3.8	0.3	11325	4.279	0.092
17	3.6	4.0	913	4.311	0.099	3.1	1.3	2379	4.233	0.086
18	3.3	1.8	1820	4.421	0.121	1.7	2.1	843	4.214	0.104
19	2.9	5.6	517	4.417	0.091	1.5	1.8	818	4.018	0.152
20	2.6	10.1	255	4.448	0.073	1.3	1.3	1027	4.272	0.169
21	2.2	6.8	322	4.650	0.087	1.1	2.1	530	4.318	0.117
22	1.8	3.2	552	4.533	0.112	0.8	3.9	193	4.052	0.184
23	1.5	3.2	471	4.225	0.134	0.6	1.5	391	3.986	0.227
24	1.3	2.3	580	4.023	0.169	0.5	0.7	687	3.815	0.267
25	1.4	2.1	665	4.506	0.145	0.4	0.7	516	4.049	0.211
26	1.4	1.1	1327	4.663	0.114	0.3	0.2	1715	4.025	0.282
27	1.2	1.4	881	4.402	0.154	0.4	nd	nd	4.504	0.298
28	0.9	1.4	685	4.130	0.151	0.5	0.5	858	4.080	0.212
29	0.9	1.2	697	4.771	0.217	0.5	0.6	860	4.314	0.280
30	0.9	1.2	744	4.205	0.169	0.5	0.3	1819	4.136	0.226

Extended Data Table 4, continued

	Inside Hole #3					Inside Hole #4				
Bin #	U (ppm)	Th (ppb)	U/Th	$^{230}Th/^{238}U$	$^{230}Th/^{238}U$ error	U (ppm)	Th (ppb)	U/Th	$^{230}Th/^{238}U$	$^{230}Th/^{238}U$ error
1	14.5	14.1	1033	4.928	0.086	14.7	2.4	6110	5.006	0.141
2	10.4	9.7	1078	4.220	0.103	12.7	7.7	1637	4.528	0.064
3	10.3	2.4	4226	3.981	0.068	11.9	7.8	1512	4.295	0.078
4	10.6	1.7	6331	3.980	0.091	11.8	3.8	3132	4.616	0.068
5	10.8	1.4	7791	4.153	0.100	11.0	0.5	21379	4.647	0.065
6	9.7	4.7	2069	3.997	0.070	10.7	11.6	921	4.538	0.062
7	9.8	2.3	4259	4.393	0.078	9.7	1.0	9534	4.299	0.058
8	6.8	17.4	389	4.363	0.081	9.1	7.1	1287	4.065	0.091
9	5.7	6.4	897	4.304	0.067	7.8	1.4	5385	4.091	0.068
10	4.9	4.9	990	4.067	0.079	8.7	0.9	9310	4.502	0.086
11	4.7	3.5	1332	4.157	0.092	7.7	1.9	3970	4.430	0.118
12	4.0	3.4	1161	4.246	0.107	7.2	3.5	2054	4.489	0.096
13	3.3	1.3	2516	4.340	0.130	6.4	5.2	1237	4.517	0.096
14	2.4	4.5	545	4.227	0.111	4.8	5.3	913	4.180	0.099
15	1.4	2.5	578	3.832	0.156	4.3	5.9	723	4.095	0.091
16	0.7	1.2	569	3.897	0.245	2.8	6.8	414	3.838	0.131
17	0.5	1.4	342	3.857	0.168	0.6	3.1	182	3.463	0.135
18	0.4	0.5	799	3.888	0.229	0.4	1.1	386	3.495	0.233
19	0.3	0.5	600	3.709	0.306	0.4	1.7	215	3.580	0.263
20	0.3	0.6	439	3.646	0.327	0.4	0.8	459	3.688	0.293
21	0.2	0.1	1828	3.727	0.478	0.3	0.5	668	3.240	0.264
22	0.2	0.0	3591	3.833	0.392	0.4	0.6	625	3.704	0.244
23	0.1	0.0	11082	3.601	0.427	0.4	0.6	798	3.780	0.258
24	0.1	0.2	901	3.616	0.563	0.4	0.4	1128	3.685	0.218
25	0.2	0.1	3853	4.118	0.368	0.4	0.6	642	3.899	0.352
26	0.3	0.9	314	3.681	0.276	0.3	0.4	687	3.350	0.379
27	0.3	0.2	1306	3.667	0.279	0.2	0.4	522	3.447	0.403
28	0.2	0.6	336	4.051	0.439	0.2	0.0	4109	3.162	0.423
29	0.2	0.0	nd	3.171	0.369	0.1	0.6	240	2.851	0.356
30	0.1	nd	nd	3.383	0.488	0.1	0.6	228	3.045	0.422

Extended Data Table 4, continued

	Inside Hole #5					Inside Hole #6				
Bin #	U (ppm)	Th (ppb)	U/Th	$^{230}Th/^{238}U$	$^{230}Th/^{238}U$ error	U (ppm)	Th (ppb)	U/Th	$^{230}Th/^{238}U$	$^{230}Th/^{238}U$ error
1	14.2	6.8	2094	5.102	0.092	13.4	12.1	1110	5.257	0.085
2	12.3	3.3	3696	4.591	0.115	12.2	7.1	1716	4.834	0.084
3	10.5	2.6	4087	4.012	0.098	11.0	4.0	2791	4.274	0.068
4	11.0	2.0	5450	3.981	0.059	10.1	2.9	3547	4.080	0.051
5	10.4	0.8	13657	4.023	0.087	9.4	9.0	1047	3.822	0.085
6	10.0	1.2	8494	3.828	0.074	9.1	1.3	7243	3.958	0.070
7	8.9	6.7	1319	3.849	0.078	8.8	11.2	779	4.218	0.085
8	8.0	5.1	1580	3.979	0.076	7.1	22.9	310	4.056	0.082
9	8.1	4.4	1847	3.992	0.062	6.9	4.4	1565	4.016	0.116
10	7.2	5.1	1422	3.925	0.084	5.8	2.0	2876	4.072	0.090
11	6.0	10.3	587	4.039	0.079	6.2	1.6	3893	4.376	0.088
12	5.2	3.9	1324	4.358	0.089	5.7	3.0	1897	4.196	0.100
13	4.2	3.0	1422	4.425	0.106	4.7	2.0	2374	3.952	0.109
14	3.4	5.3	647	4.172	0.083	4.4	1.8	2478	3.977	0.089
15	2.8	4.5	630	4.221	0.088	3.9	2.3	1658	4.138	0.122
16	1.1	3.3	330	3.839	0.202	3.7	2.0	1894	4.447	0.116
17	0.6	0.4	1459	3.610	0.203	2.9	5.2	553	4.418	0.086
18	0.9	0.9	1063	3.941	0.189	2.2	2.0	1071	4.364	0.100
19	0.9	0.8	1106	3.910	0.133	1.8	1.3	1405	4.171	0.123
20	0.7	0.8	946	3.956	0.177	1.5	2.2	701	4.102	0.129
21	0.7	0.8	845	4.012	0.201	1.5	2.3	630	4.385	0.146
22	0.6	0.4	1461	3.950	0.222	1.5	0.8	1901	4.363	0.204
23	0.5	0.5	876	3.806	0.207	1.4	0.7	2103	4.220	0.145
24	0.4	0.6	616	3.597	0.197	1.0	1.8	586	4.040	0.151
25	0.4	0.5	665	3.747	0.224	0.9	1.9	470	4.040	0.168
26	0.3	0.6	520	3.857	0.221	0.9	0.9	963	3.988	0.137
27	0.3	0.7	422	3.354	0.266	0.9	0.7	1221	4.209	0.153
28	0.3	0.7	452	3.619	0.309	0.8	0.9	930	3.979	0.189
29	0.2	0.3	698	3.346	0.313	0.7	0.2	3141	3.757	0.161
30	0.2	nd	nd	3.492	0.420	0.6	0.3	2040	3.801	0.195

Extended Data Table 4, continued

	Inside Hole #7					Inside Hole #8				
Bin #	U (ppm)	Th (ppb)	U/Th	$^{230}Th/^{238}U$	$^{230}Th/^{238}U$ error	U (ppm)	Th (ppb)	U/Th	$^{230}Th/^{238}U$	$^{230}Th/^{238}U$ error
1	12.5	5.7	2170	4.579	0.086	15.1	8.2	1839	4.088	0.050
2	12.0	2.3	5123	4.635	0.069	12.1	7.7	1578	3.991	0.055
3	10.9	9.8	1108	4.319	0.075	12.1	2.4	4986	4.128	0.066
4	10.1	16.7	609	4.324	0.062	11.7	2.2	5339	4.266	0.067
5	9.3	4.6	2025	4.285	0.069	10.4	1.7	5982	4.302	0.056
6	9.6	5.9	1618	4.136	0.082	10.5	1.8	5704	4.355	0.065
7	9.1	1.5	5990	4.208	0.073	9.2	19.0	483	4.346	0.076
8	9.3	2.0	4732	4.443	0.074	9.1	2.7	3348	4.349	0.074
9	8.4	1.0	8621	4.340	0.090	9.0	2.0	4400	4.268	0.069
10	8.1	0.9	8609	4.446	0.070	7.6	3.1	2419	4.196	0.078
11	8.2	0.7	12567	4.652	0.097	7.3	0.5	14085	4.305	0.099
12	7.1	0.8	9178	4.052	0.094	7.8	3.8	2026	4.569	0.103
13	6.6	1.1	5998	4.234	0.084	6.8	11.2	609	4.488	0.085
14	5.5	2.5	2165	4.130	0.066	5.9	7.3	813	4.384	0.101
15	5.3	1.0	5367	4.184	0.105	4.8	2.7	1772	4.215	0.135
16	4.3	5.9	729	4.377	0.121	4.5	3.4	1326	4.236	0.079
17	3.9	1.9	2122	4.345	0.105	3.6	0.7	5490	4.044	0.084
18	4.0	1.8	2228	4.455	0.119	3.8	8.9	427	4.307	0.067
19	3.2	2.9	1102	4.113	0.118	3.6	5.6	646	4.250	0.119
20	2.9	8.4	342	4.340	0.110	3.3	3.3	1000	4.799	0.128
21	2.8	4.0	693	4.522	0.096	3.3	3.0	1097	4.804	0.081
22	2.6	0.9	2823	4.498	0.112	2.9	0.3	9530	4.761	0.126
23	2.3	1.3	1821	4.453	0.114	2.7	0.5	4983	4.750	0.099
24	1.9	0.8	2323	4.138	0.119	2.2	0.3	7644	4.462	0.127
25	1.8	0.2	9733	4.215	0.147	2.2	2.2	987	4.601	0.116
26	1.8	0.5	3274	4.232	0.153	2.1	1.2	1802	4.453	0.189
27	1.7	0.9	1936	4.446	0.194	1.6	38.1	41	3.585	0.132
28	1.4	0.3	4408	4.103	0.127	0.5	20.9	26	4.031	0.168
29	1.3	0.1	21804	4.164	0.112	0.6	29.6	19	4.078	0.162
30	1.2	3.5	342	4.259	0.178	0.5	17.1	30	4.131	0.308

Extended Data Table 4, continued

	Outside Hole #1					Outside Hole #2				
Bin #	U (ppm)	Th (ppb)	U/Th	$^{230}Th/^{238}U$	$^{230}Th/^{238}U$ error	U (ppm)	Th (ppb)	U/Th	$^{230}Th/^{238}U$	$^{230}Th/^{238}U$ error
1	4.6	2.4	1931	4.290	0.085	16.9	2.2	7699	3.859	0.111
2	3.7	3.3	1148	4.291	0.068	16.8	2.9	5835	4.427	0.057
3	3.2	3.0	1057	4.347	0.088	15.2	1.9	8001	4.774	0.057
4	2.7	1.9	1424	4.269	0.111	15.1	0.4	38447	4.916	0.080
5	2.2	1.5	1411	4.320	0.083	13.5	20.8	651	4.959	0.071
6	1.9	1.0	1928	4.178	0.135	11.0	8.7	1258	4.640	0.065
7	1.6	0.5	3131	4.301	0.117	10.2	4.6	2184	4.354	0.058
8	1.2	1.1	1097	4.295	0.136	9.5	1.9	4994	4.145	0.064
9	1.1	0.8	1296	4.200	0.168	8.7	0.5	16767	4.026	0.066
10	1.0	0.3	2903	4.160	0.114	8.4	2.4	3432	4.088	0.057
11	1.0	0.5	2026	4.065	0.129	8.1	4.5	1811	4.250	0.058
12	0.8	0.9	971	3.883	0.152	6.7	2.5	2716	3.927	0.071
13	0.7	0.7	1086	3.974	0.228	6.1	0.5	12198	3.818	0.081
14	0.6	0.3	1830	3.738	0.183	5.1	0.6	8351	3.834	0.097
15	0.6	0.5	1055	3.548	0.153	4.8	1.7	2768	3.953	0.087
16	0.5	0.6	883	3.493	0.233	5.3	0.7	7762	4.528	0.123
17	0.5	0.1	3957	3.533	0.155	5.0	0.7	6801	4.561	0.079
18	0.5	0.4	1251	3.654	0.207	4.6	0.9	5081	4.484	0.075
19	0.5	0.1	3635	3.691	0.215	4.4	0.9	4797	4.482	0.080
20	0.5	0.1	5655	3.614	0.203	4.0	0.7	5786	4.332	0.062
21	0.6	5.2	111	3.389	0.186	4.3	0.8	5161	4.557	0.069
22	1.1	170.1	7	3.045	0.204	3.7	3.0	1257	4.670	0.093
23	0.7	71.1	9	3.171	0.262	3.5	2.5	1426	4.606	0.101
24	0.5	6.0	77	3.401	0.235	3.2	6.7	472	4.559	0.104
25	0.4	6.3	65	3.339	0.169	2.8	1.3	2166	4.532	0.113
26	0.4	4.6	94	3.391	0.199	2.7	1.3	2126	4.601	0.129
27	0.4	3.3	120	3.342	0.194	2.3	1.0	2345	4.415	0.100
28	0.4	2.5	162	3.238	0.208	2.0	0.7	2741	4.170	0.105
29	0.4	1.7	244	3.553	0.187	1.8	1.1	1685	4.244	0.103
30	4.6	2.4	1931	4.290	0.085	1.5	0.8	1960	4.088	0.128

Extended Data Table 4, continued

	Outside Hole #3					Outside Hole #4				
Bin #	U (ppm)	Th (ppb)	U/Th	$^{230}Th/^{238}U$	$^{230}Th/^{238}U$ error	U (ppm)	Th (ppb)	U/Th	$^{230}Th/^{238}U$	$^{230}Th/^{238}U$ error
1	15.5	4.5	3461	3.615	0.102	14.3	2.9	5016	4.117	0.103
2	12.6	2.5	5154	4.023	0.086	13.4	2.5	5414	4.310	0.070
3	15.0	3.3	4525	4.420	0.089	13.2	2.5	5360	4.501	0.049
4	14.4	3.0	4872	4.726	0.131	11.3	0.8	14299	4.370	0.054
5	13.4	1.5	8975	4.577	0.137	11.6	nd	nd	4.432	0.067
6	13.5	0.9	15358	4.656	0.075	12.5	0.6	20268	4.621	0.070
7	12.9	3.2	4019	4.900	0.071	13.0	12.0	1087	5.000	0.061
8	12.7	7.3	1739	5.119	0.097	12.2	4.5	2707	4.945	0.075
9	10.7	3.3	3219	4.821	0.087	9.7	2.1	4703	4.774	0.046
10	9.5	3.3	2834	4.626	0.132	8.6	1.0	8586	4.763	0.043
11	9.5	12.0	797	4.724	0.082	8.0	0.7	11395	4.606	0.082
12	8.4	2.9	2943	4.431	0.158	7.5	5.9	1257	4.262	0.080
13	8.5	9.3	917	4.658	0.090	7.0	4.5	1543	4.254	0.066
14	7.9	5.6	1406	4.543	0.066	6.0	1.1	5381	4.299	0.080
15	6.9	4.2	1641	4.419	0.138	5.3	0.3	20252	4.215	0.074
16	6.3	2.5	2548	4.354	0.086	4.2	nd	nd	4.083	0.074
17	5.8	1.6	3567	4.361	0.093	3.8	nd	nd	4.121	0.078
18	5.9	0.4	14010	4.298	0.101	3.6	0.1	30030	4.241	0.095
19	5.7	0.3	19984	4.253	0.128	3.2	1.1	2926	4.360	0.083
20	5.4	2.6	2053	4.363	0.077	2.6	0.8	3382	4.231	0.072
21	5.2	9.6	535	4.408	0.071	2.7	0.4	6394	4.387	0.103
22	4.8	1.5	3225	4.352	0.099	2.8	0.0	-87918	4.527	0.102
23	4.5	2.5	1784	4.463	0.103	2.4	0.3	7234	4.518	0.102
24	4.3	2.9	1506	4.443	0.179	2.0	1.0	2061	4.458	0.111
25	4.1	1.2	3471	4.733	0.114	1.7	0.6	2797	4.364	0.122
26	3.9	1.7	2319	4.705	0.105	1.7	0.1	16168	4.294	0.122
27	3.9	1.5	2576	4.388	0.102	1.6	0.1	12496	4.155	0.093
28	3.7	0.6	6110	4.558	0.086	1.4	nd	nd	4.370	0.125
29	2.4	13.8	177	4.121	0.174	1.3	0.1	8661	4.421	0.126
30	3.0	40.8	74	2.958	0.236	1.2	nd	nd	4.426	0.147

Extended Data Table 5: 2014 laser ablation $^{234}U/^{238}U$ runs on basicranial fragment. For hole positions, see Extended Data Figure 8. nd: not detemined, Th concentration below background. Errors are 2 s.d.

	Inside Hole #1					Inside Hole #2				
Bin #	U (ppm)	Th (ppb)	U/Th	$^{234}U/^{238}U$	$^{234}U/^{238}U$ error	U (ppm)	Th (ppb)	U/Th	$^{234}U/^{238}U$	$^{234}U/^{238}U$ error
1	11.6	3.5	3293	3.730	0.038	11.0	3.1	3509	3.844	0.031
2	10.1	5.9	1717	3.643	0.045	9.9	3.4	2962	3.729	0.029
3	8.9	6.9	1288	3.621	0.022	9.4	4.1	2275	3.829	0.028
4	7.1	6.0	1189	3.766	0.043	7.5	2.3	3206	3.738	0.026
5	6.8	2.6	2619	3.834	0.029	6.4	11.3	563	3.634	0.034
6	5.2	2.8	1817	3.750	0.034	5.8	5.8	1009	3.561	0.041
7	3.5	1.2	2797	3.563	0.050	5.4	4.9	1092	3.611	0.044
8	2.8	1.9	1448	3.554	0.041	4.2	2.3	1804	3.750	0.055
9	2.1	1.1	1970	3.660	0.055	2.5	4.8	517	3.381	0.048
10	1.7	1.2	1447	3.635	0.042	2.1	0.4	4606	3.591	0.048
11	1.5	1.5	1014	3.618	0.043	1.7	0.6	2853	3.515	0.064
12	1.3	1.3	996	3.702	0.055	1.3	1.4	947	3.426	0.057
13	1.0	0.4	2349	3.615	0.056	1.2	0.3	3665	3.436	0.068
14	0.7	0.6	1202	3.652	0.087	1.1	0.4	2825	3.378	0.065
15	0.4	0.6	723	3.659	0.079	0.9	0.5	1573	3.377	0.085
16	0.4	0.7	580	3.595	0.082	0.3	0.7	501	3.603	0.100
17	0.4	0.1	3074	3.642	0.101	0.2	0.0	4794	3.583	0.124
18	0.3	0.5	470	3.733	0.119	0.2	0.3	522	3.577	0.152
19	0.3	0.4	777	3.779	0.108	0.1	0.0	2550	3.673	0.141
20	0.3	0.1	2315	3.683	0.104	0.1	nd	nd	3.624	0.173
21	0.2	0.3	535	3.697	0.137	0.1	nd	nd	3.786	0.161
22	0.2	0.3	493	3.751	0.162	0.2	0.4	542	3.581	0.114
23	0.2	nd	nd	3.661	0.129	0.2	nd	nd	3.554	0.099
24	0.1	0.3	473	3.502	0.119	0.2	0.2	1047	3.540	0.119
25	0.2	0.1	1352	3.635	0.132	0.1	0.1	2603	3.563	0.154
26	0.2	0.5	321	3.685	0.140	0.1	0.2	667	3.479	0.139
27	0.2	0.2	632	3.672	0.121	0.1	0.4	145	3.798	0.312
28	0.1	nd	nd	3.558	0.125	0.0	0.1	449	3.927	0.236
29	0.1	nd	nd	3.579	0.142	0.0	nd	nd	3.777	0.308
30	0.1	nd	nd	3.586	0.158	0.0	0.1	268	3.758	0.316

Extended Data Table 5, continued

	Inside Hole #3				
Bin #	U (ppm)	Th (ppb)	U/Th	$^{234}U/^{238}U$	$^{234}U/^{238}U$ error
1	11.5	5.4	2107	3.868	0.036
2	10.1	6.1	1640	3.621	0.024
3	9.5	8.4	1132	3.602	0.036
4	8.4	4.2	2015	3.676	0.022
5	8.3	3.1	2653	3.678	0.050
6	8.1	0.9	8686	3.745	0.048
7	7.0	3.9	1814	3.706	0.042
8	5.8	3.7	1581	3.593	0.049
9	4.2	5.0	830	3.479	0.034
10	3.5	4.1	850	3.449	0.034
11	3.2	1.0	3066	3.636	0.033
12	2.7	1.1	2384	3.608	0.043
13	2.0	2.4	838	3.764	0.051
14	0.8	1.5	494	3.620	0.094
15	0.6	0.7	914	3.680	0.086
16	0.6	0.2	3303	3.799	0.071
17	0.5	1.0	536	3.731	0.083
18	0.5	0.4	1300	3.631	0.066
19	0.4	0.2	1635	3.753	0.090
20	0.3	0.6	483	3.747	0.101
21	0.2	0.7	345	3.815	0.125
22	0.2	0.4	480	3.540	0.106
23	0.2	0.2	751	3.615	0.122
24	0.2	0.5	344	3.785	0.125
25	0.2	0.2	931	3.885	0.164
26	0.1	nd	nd	3.557	0.153
27	0.2	0.6	290	3.564	0.122
28	0.2	0.1	1819	3.726	0.137
29	0.2	0.0	3486	3.716	0.145
30	0.2	0.2	1099	3.810	0.141

Extended Data Table 5, continued

	Outside Hole #1					Outside Hole #2				
Bin #	U (ppm)	Th (ppb)	U/Th	$^{234}U/^{238}U$	$^{234}U/^{238}U$ error	U (ppm)	Th (ppb)	U/Th	$^{234}U/^{238}U$	$^{234}U/^{238}U$ error
1	16.2	36.6	442	3.847	0.029	17.1	1.4	12532	4.204	0.026
2	13.8	2.7	5086	3.953	0.026	14.8	2.4	6249	4.213	0.024
3	14.1	5.3	2655	4.071	0.025	13.0	7.0	1849	4.262	0.040
4	13.6	5.0	2720	4.151	0.030	10.2	1.7	5880	3.968	0.036
5	12.8	2.2	5843	4.180	0.024	9.0	3.4	2677	4.083	0.043
6	11.9	0.2	52122	4.233	0.052	8.0	1.3	6064	4.051	0.054
7	11.2	5.8	1952	4.261	0.050	7.7	1.3	6102	3.995	0.067
8	9.5	3.0	3169	4.174	0.033	7.2	2.2	3201	3.790	0.042
9	7.1	3.8	1878	3.842	0.055	7.1	0.8	9155	3.762	0.028
10	5.9	9.1	651	3.846	0.045	6.3	2.3	2713	3.671	0.049
11	5.1	1.2	4268	3.800	0.072	6.2	12.1	510	3.819	0.060
12	5.1	1.2	4231	3.851	0.078	5.6	2.9	1926	3.896	0.048
13	4.6	1.0	4781	3.886	0.059	4.6	0.8	6081	3.793	0.055
14	3.9	0.0	120847	3.882	0.040	4.4	1.2	3798	3.867	0.038
15	3.4	0.7	4670	3.888	0.034	4.3	1.5	2924	3.982	0.053
16	3.0	0.8	3878	3.792	0.041	3.7	0.7	5359	3.888	0.040
17	2.9	0.5	5961	3.884	0.058	3.5	0.5	7285	4.043	0.075
18	3.0	0.8	3628	4.061	0.050	2.9	0.8	3534	3.991	0.062
19	2.3	nd	nd	3.923	0.052	2.2	0.1	18043	3.891	0.066
20	2.0	nd	nd	3.858	0.058	1.9	0.2	7619	3.826	0.052
21	1.6	5.4	298	3.917	0.051	1.6	0.7	2265	3.793	0.073
22	1.5	1.0	1450	3.966	0.062	1.2	0.7	1652	3.554	0.045
23	1.4	nd	nd	3.912	0.053	0.9	0.7	1332	3.723	0.059
24	1.3	0.7	1977	3.884	0.056	0.9	0.4	1994	3.891	0.059
25	1.3	0.5	2698	3.961	0.061	0.8	0.0	29135	3.881	0.089
26	1.1	0.5	2277	3.996	0.060	0.8	nd	nd	3.874	0.073
27	1.0	nd	nd	4.104	0.065	0.7	nd	nd	3.873	0.087
28	0.9	0.0	1327573	4.077	0.057	0.7	0.1	12793	3.878	0.070
29	0.8	0.1	8549	4.069	0.082	0.6	0.0	12791	3.926	0.079
30	0.7	nd	nd	4.128	0.074	0.6	0.1	7682	3.832	0.067

Extended Data Table 5, continued

	Outside Hole #3					Outside Hole #4				
Bin #	U (ppm)	Th (ppb)	U/Th	$^{234}U/^{238}U$	$^{234}U/^{238}U$ error	U (ppm)	Th (ppb)	U/Th	$^{234}U/^{238}U$	$^{234}U/^{238}U$ error
1	20.1	5.6	3587	4.312	0.025	22.1	8.8	2512	4.285	0.022
2	16.8	8.8	1894	4.363	0.027	19.6	6.0	3267	4.314	0.018
3	13.0	5.1	2541	4.176	0.046	17.1	2.8	6040	4.330	0.021
4	10.6	3.3	3245	3.928	0.029	14.6	2.2	6492	4.247	0.024
5	9.7	6.8	1425	3.830	0.040	12.3	3.9	3143	4.140	0.032
6	9.0	4.5	2013	3.710	0.022	11.2	4.7	2356	4.114	0.036
7	8.7	9.0	973	3.771	0.031	9.9	0.9	10720	3.988	0.062
8	8.3	6.1	1350	3.828	0.025	8.6	0.8	11218	3.872	0.026
9	7.6	2.1	3646	3.761	0.042	7.7	14.0	547	3.867	0.033
10	6.9	3.5	1942	3.743	0.029	6.7	7.8	863	3.716	0.034
11	5.9	2.4	2492	3.622	0.027	6.6	1.1	6056	3.798	0.045
12	4.7	1.3	3654	3.488	0.034	5.8	1.4	4138	3.679	0.022
13	4.3	1.4	3083	3.573	0.046	5.2	1.2	4436	3.695	0.028
14	4.3	3.1	1380	3.701	0.052	4.6	1.5	3126	3.529	0.039
15	3.8	5.6	688	3.763	0.042	4.1	0.5	7596	3.668	0.043
16	3.2	3.4	950	3.662	0.044	3.6	0.5	7552	3.742	0.035
17	2.9	1.6	1877	3.628	0.060	3.6	0.5	6600	3.964	0.067
18	2.5	0.9	2870	3.606	0.049	3.5	0.4	9380	3.923	0.028
19	2.3	1.0	2311	3.781	0.080	3.1	0.4	8560	3.986	0.074
20	2.0	0.7	2867	3.867	0.048	2.7	0.5	4894	3.788	0.059
21	1.6	0.5	3198	3.916	0.062	2.2	0.5	4110	3.634	0.044
22	1.4	0.9	1495	3.800	0.072	1.8	0.7	2554	3.746	0.040
23	1.2	0.2	6565	3.806	0.063	2.0	0.6	3539	3.739	0.041
24	1.1	0.5	2312	4.022	0.062	1.9	1.1	1662	3.829	0.059
25	1.0	0.9	1084	3.884	0.051	1.7	0.2	8870	3.936	0.071
26	0.8	nd	nd	3.801	0.073	1.6	0.4	3899	3.830	0.067
27	0.7	0.1	4908	3.843	0.107	1.3	nd	nd	3.754	0.052
28	0.6	0.2	4016	3.836	0.070	1.2	0.0	139708	3.707	0.071
29	0.7	0.3	1997	3.900	0.073	1.3	0.4	2996	3.728	0.064
30	0.4	nd	nd	3.804	12.542	1.3	nd	nd	3.808	0.053

Extended Data Table 6: Averaged $^{230}Th/^{238}U$ and $^{234}U/^{238}U$ depth profiles (from Extended Data Tables 4 and 5) and age calculations, see Extended Data Figure 8. Errors on individual measurements are 2 s.d. (excluding error of the standard, which is a correlated error for all individual measurements). Errors on averages are combined 2-s.d. of the error of the mean and error of the standard.

Inside Holes	$^{230}Th/^{238}U$	$^{230}Th/^{238}U$ error	$^{234}U/^{238}U$	$^{234}U/^{238}U$ error	Age (ka)	Age error (ka)	Initial $^{234}U/^{238}U$	$^{234}U/^{238}Ui$ error
1	4.843	0.141	3.814	0.043	468	106	11.549	3.089
2	4.529	0.101	3.665	0.033	404	52	9.343	1.197
3	4.258	0.114	3.684	0.073	305	35	7.353	0.547
4	4.267	0.100	3.727	0.026	295	24	7.269	0.404
5	4.192	0.085	3.715	0.061	282	23	7.015	0.320
6	4.124	0.081	3.686	0.062	275	22	6.842	0.286
7	4.200	0.066	3.627	0.042	309	21	7.275	0.325
8	4.249	0.072	3.632	0.060	320	28	7.486	0.426
9	4.167	0.049	3.507	0.082	343	38	7.594	0.530
10	4.219	0.072	3.558	0.056	338	32	7.648	0.512
11	4.315	0.070	3.590	0.038	357	30	8.090	0.557
12	4.296	0.071	3.579	0.081	355	45	8.029	0.718
13	4.327	0.066	3.605	0.095	354	48	8.079	0.751
14	4.190	0.047	3.550	0.087	333	37	7.519	0.478
15	4.166	0.063	3.572	0.098	318	38	7.301	0.472
16	4.185	0.102	3.665	0.067	293	30	7.102	0.432
17	4.035	0.127	3.652	0.043	266	26	6.615	0.383
18	4.136	0.118	3.647	0.046	287	29	6.958	0.446
19	4.021	0.099	3.735	0.032	247	17	6.485	0.248
20	4.156	0.138	3.685	0.035	282	30	6.953	0.489
21	4.207	0.184	3.766	0.035	273	36	6.975	0.596
22	4.212	0.134	3.624	0.065	312	41	7.336	0.662
23	4.103	0.135	3.610	0.031	290	32	6.919	0.515
24	3.922	0.106	3.609	0.089	254	26	6.348	0.298
25	4.147	0.102	3.694	0.098	278	31	6.902	0.387
26	4.031	0.149	3.574	0.060	284	36	6.736	0.541
27	3.952	0.171	3.678	0.068	246	31	6.361	0.428
28	3.894	0.119	3.737	0.107	227	24	6.196	0.251
29	3.807	0.228	3.691	0.058	222	33	6.034	0.449
30	3.806	0.160	3.718	0.068	218	23	6.027	0.303
Averages								
3-26	4.172	0.101	3.637	0.074	298	34	7.122	0.475

Extended Data Table 6, continued

Outside Holes	$^{230}Th/^{238}U$	$^{230}Th/^{238}U$ error	$^{234}U/^{238}U$	$^{234}U/^{238}U$ error	Age (ka)	Age error (ka)	Initial $^{234}U/^{238}U$	$^{234}U/^{238}Ui$ error
1	3.864	0.145	4.162	0.215	175	22	6.182	0.205
2	4.254	0.120	4.176	0.104	212	18	6.783	0.221
3	4.565	0.107	4.170	0.048	253	18	7.481	0.297
4	4.671	0.160	4.016	0.059	306	39	8.148	0.738
5	4.656	0.157	4.031	0.090	299	40	8.041	0.702
6	4.639	0.010	3.998	0.133	304	36	8.063	0.405
7	4.752	0.201	4.009	0.123	327	65	8.571	1.220
8	4.737	0.300	3.931	0.106	351	101	8.886	2.142
9	4.540	0.257	3.789	0.023	347	81	8.416	1.680
10	4.492	0.206	3.753	0.044	346	67	8.304	1.352
11	4.527	0.142	3.747	0.054	360	55	8.581	1.112
12	4.207	0.148	3.745	0.112	278	40	7.011	0.539
13	4.244	0.243	3.750	0.080	284	54	7.128	0.883
14	4.225	0.208	3.817	0.050	265	39	6.953	0.627
15	4.196	0.135	3.878	0.055	248	23	6.801	0.349
16	4.322	0.129	3.781	0.057	293	32	7.350	0.522
17	4.348	0.127	3.852	0.105	280	35	7.288	0.487
18	4.341	0.074	3.886	0.122	271	30	7.205	0.308
19	4.365	0.066	3.865	0.037	280	16	7.323	0.241
20	4.309	0.040	3.850	0.011	273	8	7.161	0.130
21	4.451	0.054	3.875	0.036	295	15	7.619	0.234
22	4.516	0.092	3.773	0.104	345	50	8.346	0.826
23	4.529	0.042	3.814	0.047	334	21	8.215	0.330
24	4.487	0.036	3.932	0.039	288	12	7.619	0.164
25	4.543	0.106	3.909	0.023	307	25	7.916	0.483
26	4.533	0.123	3.890	0.049	310	32	7.932	0.593
27	4.319	0.082	3.940	0.072	257	19	7.066	0.244
28	4.366	0.112	3.930	0.064	266	24	7.215	0.354
29	4.262	0.087	3.965	0.045	243	15	6.892	0.217
30	3.824	0.444	3.922	0.090	194	49	6.057	0.679
Averages								
4-26	4.462	0.108	3.865	0.079	301	37	7.696	0.557

Extended Data Table 7: U-series results on the Broken Hill Femur midshaft (EM793). nd: not detemined, Th concentration below background. Errors on individual measurements are 2 s.d. (excluding error of the standard, which is a correlated error for all individual measurements). Errors on averages are combined 2-s.d. of the error of the mean and error of the standard.

	U (ppm)	Th (ppb)	U/Th	$^{230}Th/^{238}U$	$^{230}Th/^{238}U$ error	$^{234}U/^{238}U$	$^{234}U/^{238}U$ error	Age (ka)	Age error (ka)
1	41.2	15.3	2693	2.270	0.049	2.840	0.035	138	6
2	43.2	7.3	5918	2.260	0.049	2.870	0.035	135	6
3	41.8	5.0	8360	2.150	0.047	2.920	0.035	120	5
4	40.0	2.4	16667	2.250	0.049	2.960	0.036	127	5
5	37.8	nd	nd	2.260	0.050	2.970	0.036	127	5
6	39.3	nd	nd	2.710	0.057	2.950	0.036	178	9
7	38.3	7.7	4974	2.610	0.056	2.900	0.036	171	8
8	35.4	nd	nd	2.570	0.056	2.950	0.036	160	8
9	34.2	1.6	21375	2.600	0.057	2.940	0.036	165	8
10	33.1	35.2	940	2.560	0.056	2.960	0.037	158	7
11	32.2	6.7	4806	2.590	0.057	2.920	0.036	166	8
12	32.4	nd	nd	2.600	0.057	2.950	0.037	164	8
13	31.6	8.2	3854	2.590	0.057	2.940	0.037	164	8
14	30.6	38.2	801	2.470	0.055	2.950	0.037	149	7
15	33.0	41.1	803	2.600	0.057	2.760	0.035	189	10
16	27.8	6.1	4557	2.340	0.054	2.970	0.037	134	6
17	26.8	10.6	2528	2.500	0.057	2.920	0.038	156	8
18	27.7	9.9	2798	2.250	0.052	2.890	0.037	132	6
19	25.8	2.6	9923	2.350	0.055	2.790	0.036	152	7
20	26.9	7.8	3449	2.540	0.058	2.930	0.037	159	8
21	25.3	4.1	6171	2.620	0.060	2.840	0.037	180	10
22	24.6	15.2	1618	2.750	0.063	2.970	0.038	181	10
23	24.3	19.0	1279	2.690	0.062	2.950	0.038	175	9
24	22.6	22.7	996	2.700	0.063	2.850	0.037	190	11
25	21.9	nd	nd	2.670	0.063	2.960	0.039	171	9
26	21.8	35.6	612	2.730	0.064	2.860	0.037	193	11
27	23.2	4.5	5156	2.800	0.064	2.980	0.039	186	10
28	23.6	8.8	2682	2.720	0.063	2.990	0.039	174	9
29	23.5	19.9	1181	2.710	0.063	2.920	0.038	182	10
30	25.4	7.1	3577	2.630	0.060	2.940	0.038	169	9
31	27.1	4.5	6022	2.660	0.060	2.930	0.038	174	9
32	28.2	13.3	2120	2.810	0.062	2.920	0.037	196	11
33	29.1	10.0	2910	2.740	0.061	2.950	0.037	182	10
AVERAGE VALUES									
	initial $^{234}U/^{238}U$	$^{234}U/^{238}U$i error		$^{230}Th/^{238}U$	$^{230}Th/^{238}U$ error	$^{234}U/^{238}U$	$^{234}U/^{238}U$ error	Age (ka)	Age error (ka)
1-33	4.032	0.071		2.555	0.066	2.919	0.038	162	9
6-33*	4.092	0.072		2.611	0.062	2.921	0.038	169	9

Younger ages for 1-5 may be due to secondary overprint

Extended Data Table 8: Gamma spectrometric results (in italics: average TIMS results from Extended DataTable 3). Errors are 2 s.d..

$^{230}Th/^{238}U$	$^{230}Th/^{238}U$ error	$^{234}U/^{238}U$	$^{234}U/^{238}U$ error	Th/U Age (ka)	Age error (ka)	$^{231}Pa/^{235}U$	$^{231}Pa/^{235}U$ error	Pa/U Age (ka)	Age error (ka)
Femur Midshaft (EM793)									
2.722	0.061	*2.924*	*0.035*	183	10	1.042	0.023	∞	
Femur Head (E907)									
2.610	0.064	*2.942*	*0.003*	166	8	1.045	0.028	∞	
Pelvis (E719)									
2.316	0.062	*2.632*	*0.002*	166	9	0.953	0.030	145	+48/-23

Extended Data Table 9: U-series results on the Broken Hill Tibia (E691). Errors on individual measurements are 2 s.d. (excluding error of the standard, which is a correlated error for all individual measurements). Errors on averages are combined 2-s.d. of the error of the mean and error of the standard.

Tibia Cross Section 1	U (ppm)	Th (ppb)	U/Th	$^{230}Th/^{238}U$	$^{230}Th/^{238}U$ error	$^{234}U/^{238}U$	$^{234}U/^{238}U$ error	Age (ka)	Age error (ka)
1	11.07	3.3	3320	4.143	0.063	4.129	0.027	206	8
2	10.15	3.4	2940	3.997	0.125	4.174	0.025	186	12
3	9.17	8.7	1050	3.641	0.110	4.082	0.030	163	9
4	6.66	15.1	440	3.889	0.109	3.966	0.042	197	13
5	7.56	5.7	1330	3.505	0.124	3.922	0.031	164	11
6	7.14	7.4	950	3.290	0.075	3.740	0.030	160	7
7	8.25	5.1	1600	3.987	0.073	3.998	0.024	204	9
8	8.59	3.4	2560	3.740	0.117	3.940	0.021	184	12
9	8.12	2.8	2930	3.698	0.089	4.068	0.026	168	8
10	8.59	1.9	4430	3.944	0.064	3.971	0.027	202	8
11	8.33	5.3	1570	3.699	0.075	4.085	0.025	167	7
12	8.85	8.2	1070	3.298	0.062	4.036	0.025	139	5
13	9.57	7.3	1300	3.670	0.063	3.801	0.029	191	8
14	8.80	2.7	3220	3.708	0.084	3.832	0.026	192	9
15	8.53	4.6	1830	3.650	0.065	3.779	0.034	191	8
16	9.79	8.3	1170	3.848	0.064	3.923	0.027	197	8
17	8.81	15.4	570	3.928	0.056	4.003	0.028	197	7
18	9.75	3.0	3220	3.725	0.079	3.883	0.037	188	9
AVERAGE VALUES									
	initial $^{234}U/^{238}U$	$^{234}U/^{238}U$i error		$^{230}Th/^{238}U$	$^{230}Th/^{238}U$ error	$^{234}U/^{238}U$	$^{234}U/^{238}U$ error	Age (ka)	Age error (ka)
1-18	5.880	0.120		3.752	0.093	3.963	0.028	183	9

Tibia Cross Section 2	U (ppm)	Th (ppb)	U/Th	$^{230}Th/^{238}U$	$^{230}Th/^{238}U$ error	$^{234}U/^{238}U$	$^{234}U/^{238}U$ error	Age (ka)	Age error (ka)
1	9.03	3.8	2360	3.062	0.066	4.089	0.023	121	4
2	9.18	4.8	1920	3.464	0.156	4.130	0.019	146	11
3	9.01	13.3	670	3.694	0.073	3.668	0.038	210	11
4	8.04	2.6	3090	3.523	0.070	4.025	0.025	157	6
5	8.13	2.5	3240	3.727	0.106	3.965	0.024	180	10
6	8.23	6.7	1230	3.537	0.057	3.984	0.026	162	5
7	6.27	3.0	2090	3.660	0.093	4.075	0.031	165	8
8	6.73	2.4	2770	3.667	0.063	4.077	0.033	165	6
9	7.95	1.3	5900	3.805	0.082	4.095	0.029	176	8
10	7.03	5.5	1280	3.551	0.082	4.157	0.031	150	6
11	6.35	3.9	1610	3.732	0.058	3.977	0.029	179	6
12	7.24	3.7	1970	3.691	0.088	3.987	0.036	175	9
13	7.26	3.4	2140	3.554	0.072	4.010	0.029	161	6
14	8.65	5.4	1580	3.921	0.071	3.726	0.035	233	12
15	8.32	5.0	1650	3.803	0.063	4.102	0.025	175	6
16	8.50	3.3	2550	3.774	0.074	4.080	0.028	174	7
17	7.93	4.3	1840	3.816	0.059	3.944	0.033	191	7
18	7.95	1.5	5260	3.729	0.086	3.947	0.040	182	9
AVERAGE VALUES									
	initial $^{234}U/^{238}U$	$^{234}U/^{238}U$i error		$^{230}Th/^{238}U$	$^{230}Th/^{238}U$ error	$^{234}U/^{238}U$	$^{234}U/^{238}U$ error	Age (ka)	Age error (ka)
3-18*	5.914	0.117		3.703	0.091	4.002	0.030	175	9

*Holes 1-2 show signs of secondary overprint

Extended Data Table 10: Summary of laser ablation results on small mammals extracted from the sediment inside the skull and its surroundings. Errors on individual measurements are 2 s.d. (excluding error of the standard, which is a correlated error for all individual measurements). Errors on averages are combined 2-s.d. of the error of the mean and error of the standard.

	$^{230}Th/^{238}U$	$^{230}Th/^{238}U$ error	$^{234}U/^{238}U$	$^{234}U/^{238}U$ error	Age (ka)	Age error (ka)	initial $^{234}U/^{238}U$	$^{234}U/^{238}Ui$ error
small mammals inside skull								
2010i-A	2.579	0.117	3.272	0.078	133	12	4.309	0.113
2010i-B	2.858	0.132	3.223	0.077	164	16	4.534	0.150
2010i-C	2.695	0.122	3.201	0.063	150	13	4.356	0.122
2010i-D	2.497	0.114	3.061	0.074	142	13	4.077	0.113
2016i-A1*	2.383	0.059	2.913	0.048	143	8	3.868	0.062
2016i-A2	2.324	0.059	2.913	0.048	137	7	3.819	0.061
2016i-B2*	5.603	0.142	4.749	0.052	311	29	10.005	0.705
2016i-C1	2.290	0.057	2.998	0.039	128	6	3.863	0.053
2016i-C2	2.234	0.055	2.998	0.039	122	6	3.822	0.051
2016i-D1	1.985	0.055	2.975	0.015	103	4	3.643	0.034
2016i-D2*	2.092	0.053	3.029	0.035	109	5	3.757	0.046
small mammals outside skull								
2016o-A1	2.371	0.059	2.966	0.065	138	8	3.899	0.070
2016o-A2	2.329	0.058	2.966	0.065	133	8	3.865	0.070
2016o-B1	2.524	0.064	3.118	0.042	140	7	4.144	0.063
2016o-B2	2.434	0.060	3.118	0.042	132	6	4.071	0.058
2016o-C1	2.214	0.055	3.146	0.052	112	5	3.940	0.059
2016o-C2	2.289	0.056	3.146	0.052	118	6	3.990	0.060
2016o-D1	2.181	0.054	2.902	0.032	124	6	3.703	0.047
2016o-D2	2.180	0.055	2.902	0.032	124	6	3.701	0.047
2016o-E1	2.120	0.055	3.146	0.037	111	5	3.931	0.048
2016o-E2	2.187	0.054	3.156	0.037	111	5	3.923	0.048
2016o-F1	2.272	0.056	3.242	0.038	111	5	4.063	0.049
2016o-F2	2.281	0.056	3.242	0.050	111	5	4.069	0.050
2016o-G1	2.230	0.056	3.214	0.056	110	5	4.012	0.062
2016o-G2	2.248	0.056	3.214	0.056	110	5	4.023	0.061
2016o-H1	2.254	0.056	3.157	0.030	114	5	3.976	0.045
2016o-H2	2.079	0.054	3.147	0.030	101	4	3.868	0.042
2016o-I1	2.227	0.057	3.358	0.032	102	4	4.142	0.045
2016o-I2	2.403	0.060	3.358	0.032	114	5	4.253	0.049
2016o-J1	2.203	0.055	2.839	0.036	131	6	3.665	0.051
2016o-J2	2.278	0.057	2.839	0.036	139	7	3.723	0.054
Average Cluster 1[#]	2.400	0.068	3.014	0.037	136	7	3.958	0.062
Average Cluster 2[#]	2.198	0.052	3.187	0.070	108	5	3.967	0.071

Supplementary Table 11: Sediment analysis (detection limits: K: 20 ppm; Th: 0.01 ppm; U:0.01 ppm)

Sample	Description	U(ppm)	Th(ppm)	K(ppm)	β-DR* (μGy/a)	γ-DR* (μGy/a)	Effective β DR$ (μGy/a)	Effective γ-DR# (μGy/a)	Effective external DR (μGy/a)
E686S1	in skull, fine	2.26	1.06	270	380	310	41	223	264
E686S2	in skull coarse	4.32	1.78	332	705	576	77	414	491
E686	**sediment inside skull**			**Average**	**543**	**443**	**59**	**319**	**378**
1	laminar deposit (hide)	12.99	0.24	116	1909	1464	209	1052	1262
2	grey sediment	17.79	9.12	1470	2962	2459	322	1770	2092
3	brown lose sediment	6.82	9.55	1177	1352	1248	145	900	1045
4	dark solidified sediment	6.75	8.17	1258	1310	1176	141	848	989
5	rust coloured sediment	14.84	1.17	174	2208	1717	242	1234	1476
6	brown sediment	3.59	9.43	2286	967	909	102	657	759
7	Breccia E556B	4.3	13.32	3302	1259	1200	133	867	1000
8	Breccia w. artefact	7.66	8.6	434	1389	1278	150	921	1071
9	Breccia w. tooth	2.17	4.73	1928	601	517	63	373	437
10	grey breccia	2.89	2.14	496	520	437	56	315	371
11	grey breccia	7.42	7.16	1557	1404	1210	151	872	1023
12	brown breccia	19.64	11.2	670	3225	2745	351	1976	2327
13	brown breccia	4.2	5.58	1122	856	764	92	551	643
14	brown breccia	3.66	2.28	525	638	531	69	382	451
15	brown rock	99.21	16.86	536	14965	11893	2148	11060	13208
16	red rust rock	26.38	0.24	200	3866	2960	556	2753	3309
17	dark brown rock	55.86	10.89	491	8480	6768	1217	6294	7511
18	brown rock	5.99	9.32	1768	1272	1159	178	1078	1256
19	rock	1.76	3.01	301	364	348	51	324	375
20	red rock	9.87	5.66	945	1670	1396	238	1298	1536

* infinite matrix dose rate

$ beta dose rate corrected for 2π geometry, attenuation for a 1000μm enamel layer and 20% water

gamma dose rate corrected for 7% self irradiation by the skull; and 20% water content (except rocks)

Extended Data Table 12: US-ESR analysis (Errors: 1 s.d.)

Skull:	Weight: 1112 g; volume: 636 cm^3;average U: 12.86±0.54 ppm $^{230}Th/^{238}U$: 4.307±0.056, $^{234}U/^{238}U$: 3.752±0.038, 20±10% water
	Closed system gamma self dose: 106±6.6 Gy (with 10±5% water)
gamma shielding[#]: 0.0764 (U), 0.069 (Th); 0.063 (K)	
X-ray and CT scanning: 60±20 Gy**	
Remaining dose after subtraction of selfdose and CT scanning: 608±25	
Enamel:	774±13 Gy[@]; 1.02±0.10 ppm U; 0.13±0.02 alpha efficiency[*]; 1000±100 µm thickness[$]
Dentine:	10.1±1.0 ppm U, 10±5% water
$^{234}U/^{238}U$:	4.491±0.009
$^{230}Th/^{238}U$:	4.623±0.017
Sediment:	3.29±1.03 ppm U; 1.42±0.36 ppm Th, 0.03±0.01 % K
Water:	20±10%

[#] Calculated after Nathan and Grün (2003)
[@] See Joannes-Boyau and Grün (2011)
[*] Grün and Katzenberger-Apel (1994)
[$] Beta attenuation calculated after Marsh (1999)
** Duval and Martin-Frances (2017)

ESR DATA Results (Errors: 1 s.d.):

Remaining dose	608±25 Gy
Gamma dose rate, sediment	318±71 µGy a^{-1}
Beta dose rate, sediment	58±19 µGy a^{-1}
Internal dose rate:	1529±307 µGy a^{-1}
Beta dose rate, dentine:	463±84 µGy a^{-1}
Total dose rate:	2369±326 µGy a^{-1}
p-values enamel/dentine	-0.93±0.05
Age:	256+33/-26 ka

Extended Data Table 13: ESR modeling

External dose modelling (Errors: 2 s.d.)

Closed system skull gamma dose	106±13 Gy
Closed system alpha and beta dose	442±57
X-ray and CT scanning	60±40 (Duval and Martín-Francés, 2017)
External dose component	166±75
Dose rate Model 1	1708 (minus 870) μGy a^{-1}
Dose rate Model 2	1284 (minus 523) μGy a^{-1}
Dose rate Model 3	1953 (minus 1085) μGy a^{-1}
Dose rate Model 4	875 (minus 415) μGy a^{-1}
Possible age range (Model 1)	<163 ka
Possible age range (Model 2)	<208 ka
Possible age range (Model 3)	<146 ka
Possible age range (Model 4,)	<312 ka

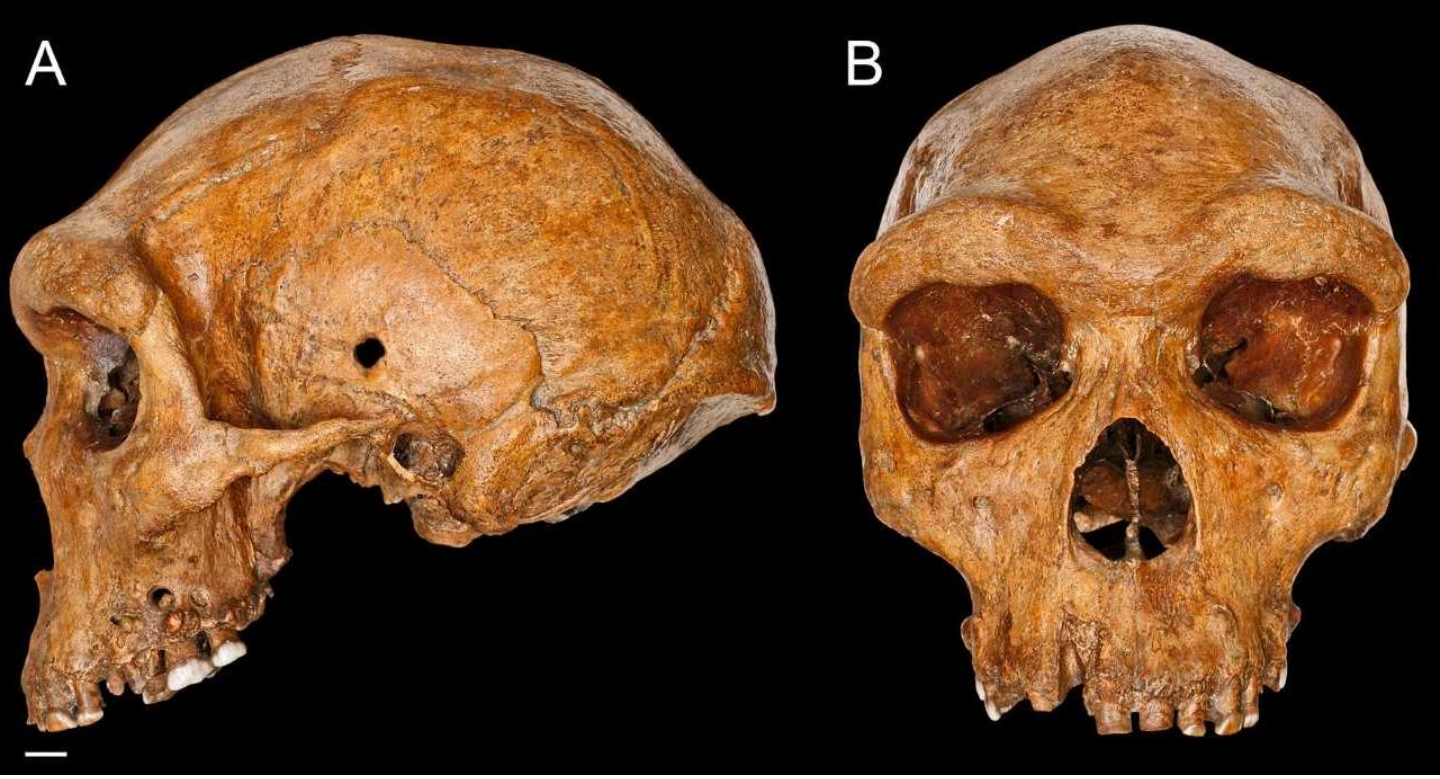
A
B

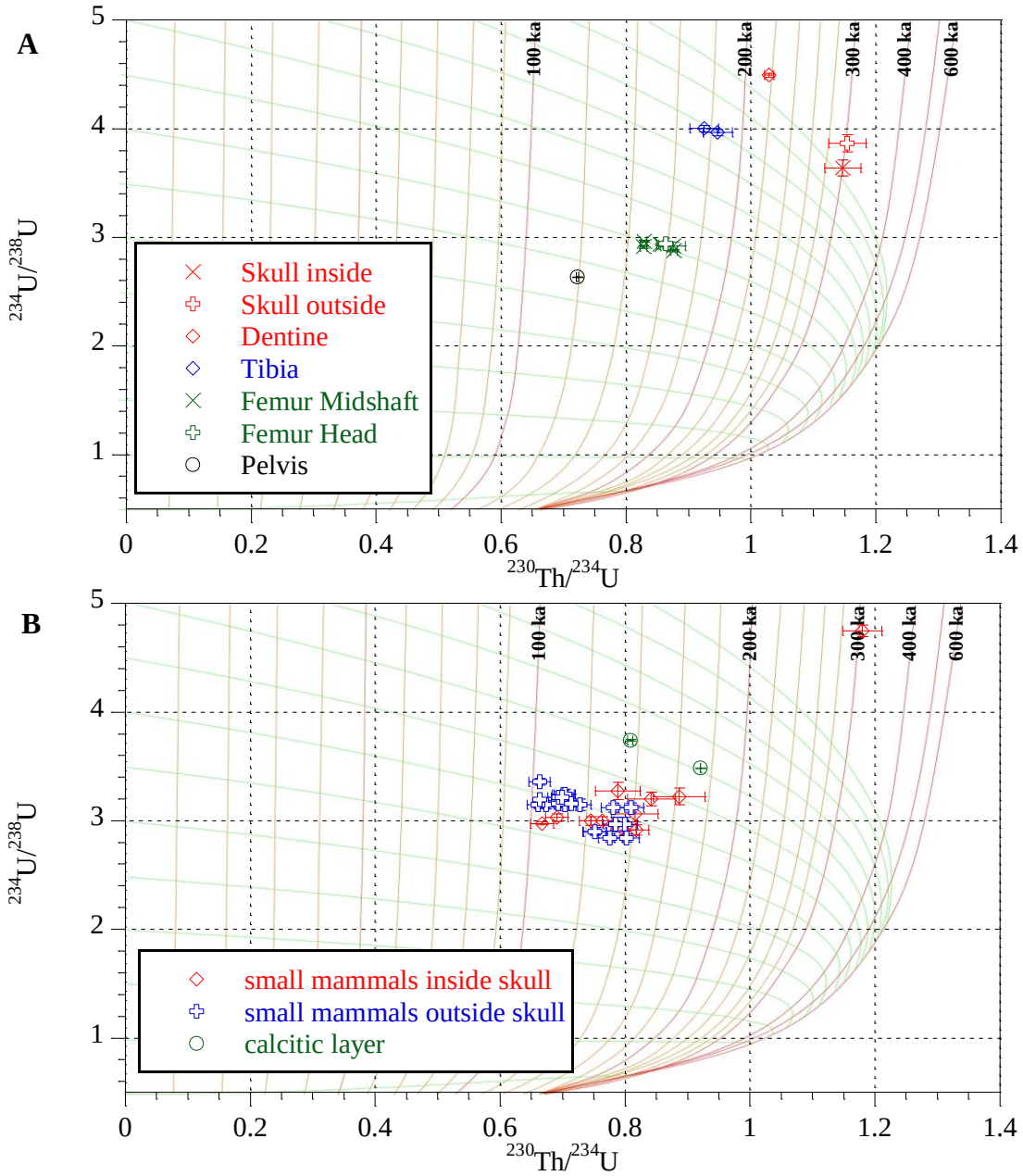

Grün et al. Figure 2

Mr. Zwigelaar, the discoverer of the Rhodesian skull, shortly after the find was made. (Photograph given Hrdlička by Mr. Zwigelaar, 1925.)

Grün et al. Extended Data Figure 1

The Rhodesian or Broken Hill cave shortly after the discovery of the skull. (After The London Illustrated News.)

Grün et al. Extended Data Figure 2

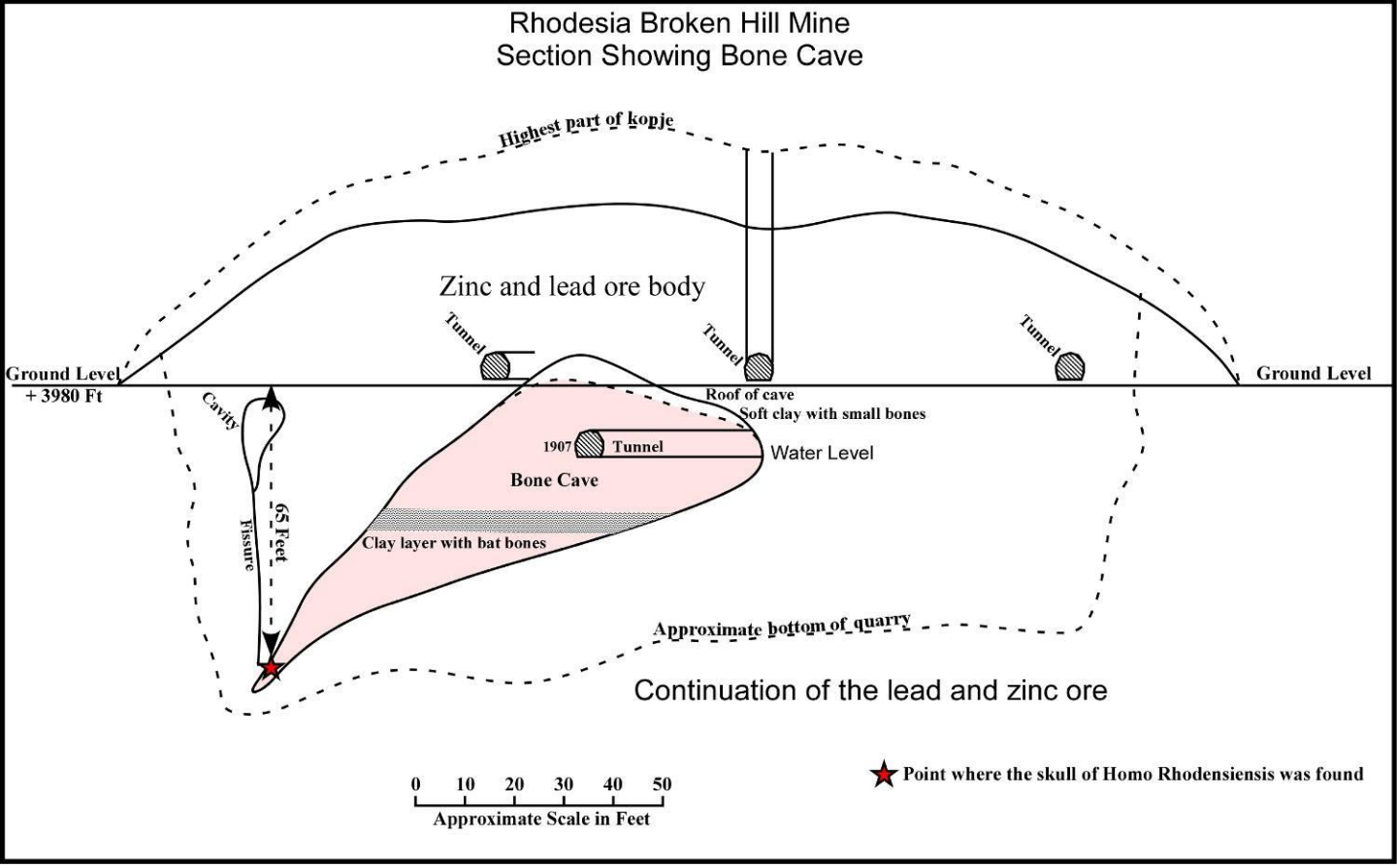

Grün et al. Extended Data Figure 3

Grün et al. Extended Data Figure 4

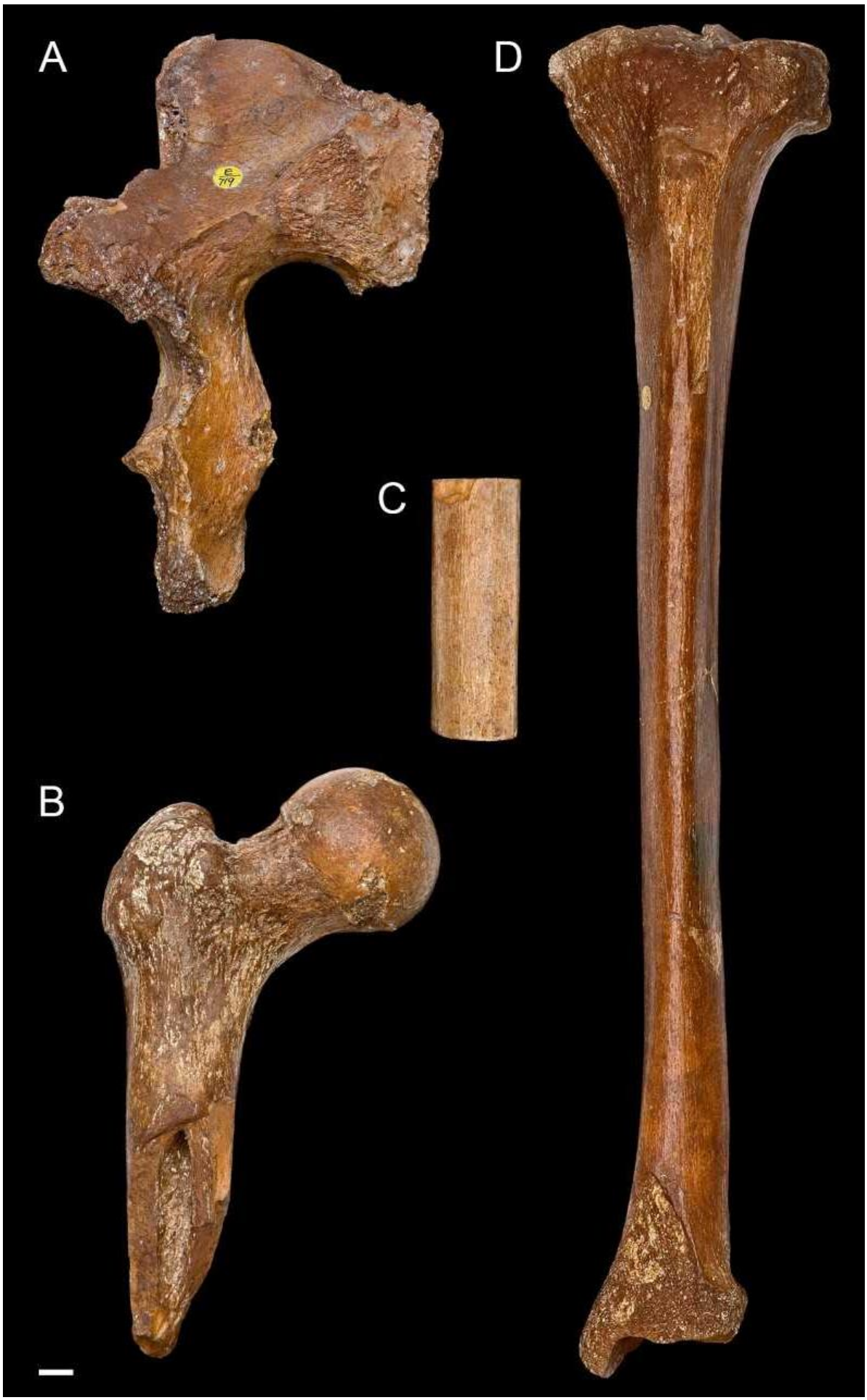

Grün et al. Extended Data Figure 5

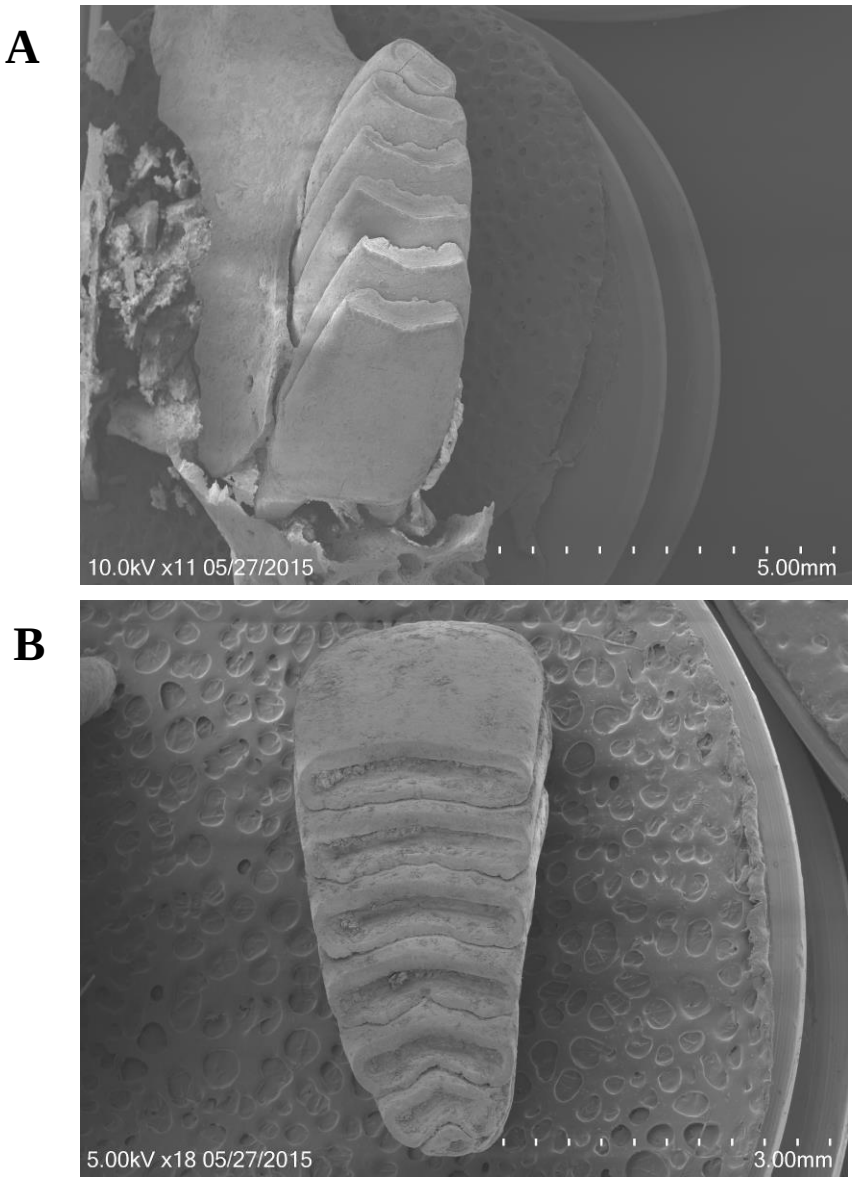

Grün et al. Extended Data Figure 6

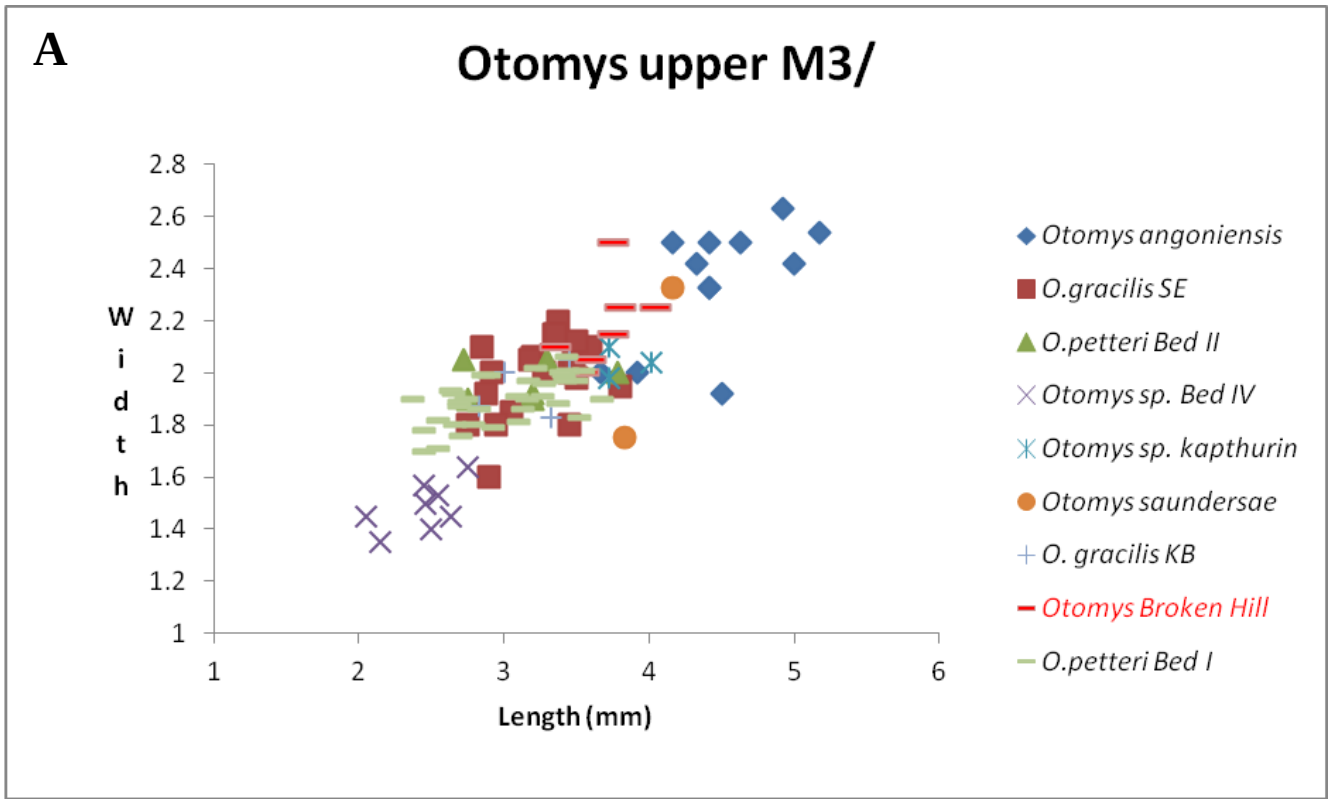

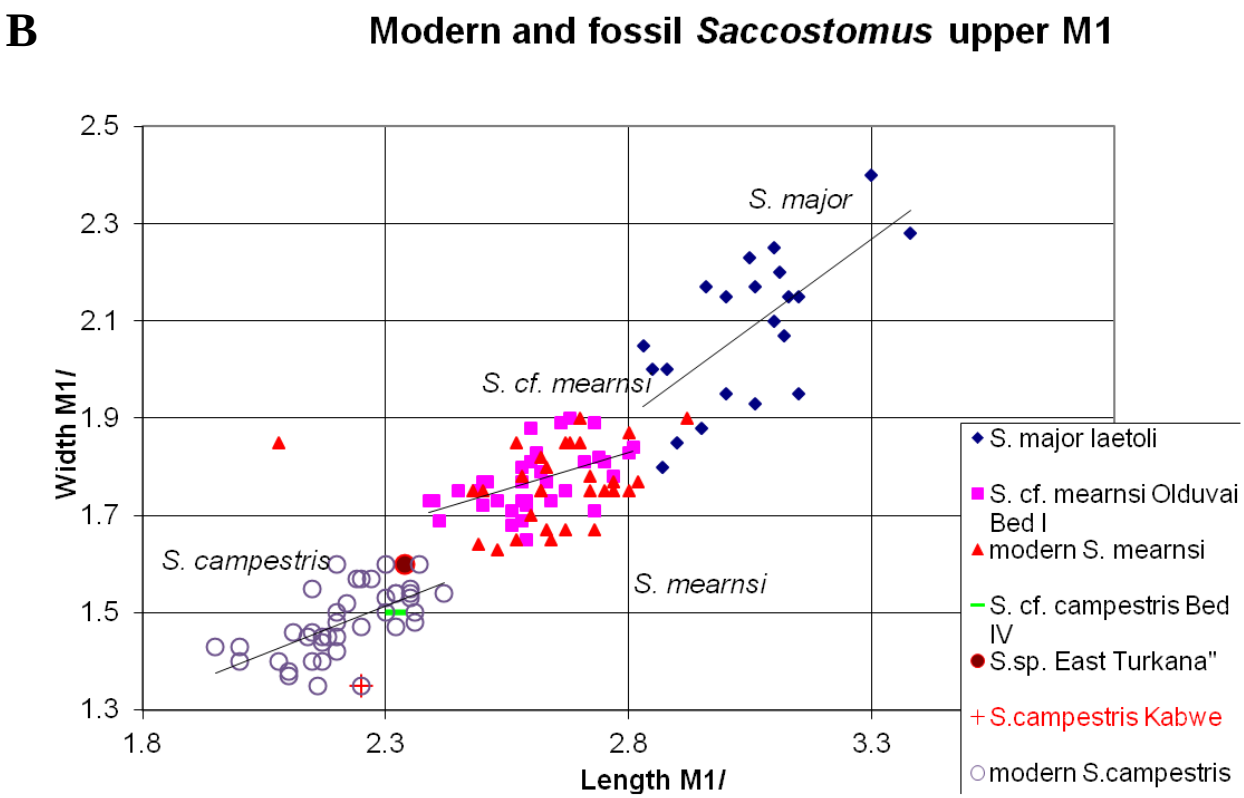

Grün et al. Extended Data Figure 7

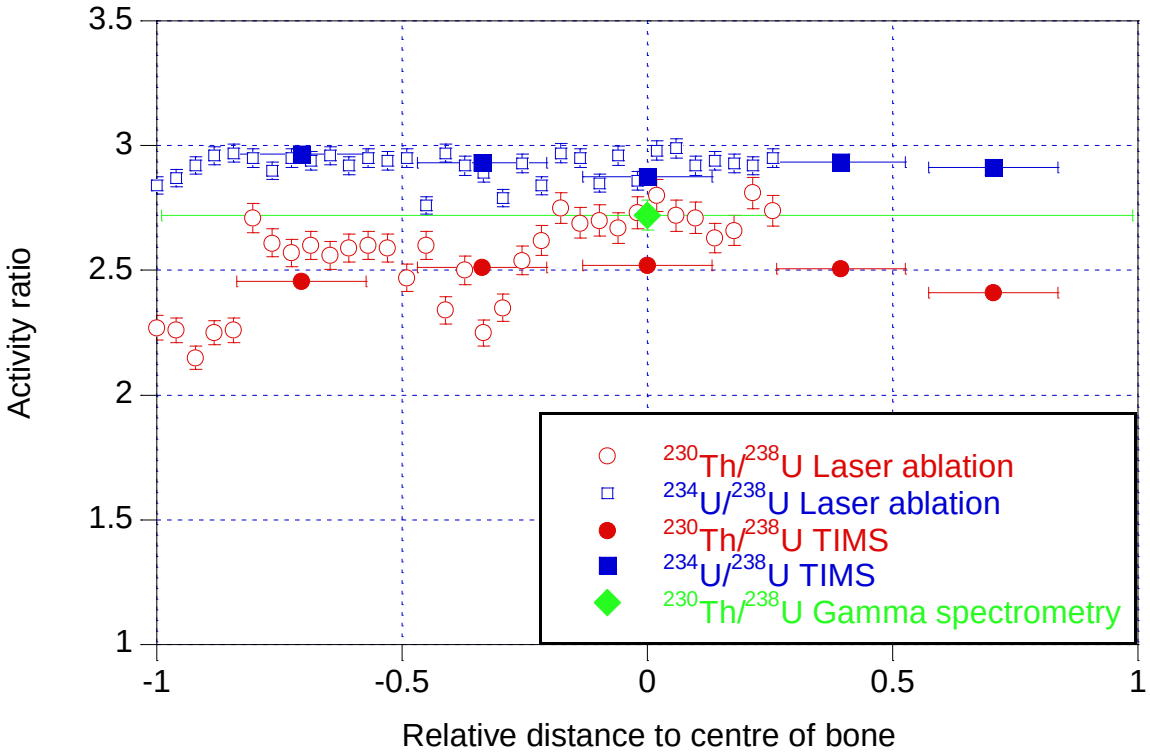

Grün et al. Extended Data Figure 8

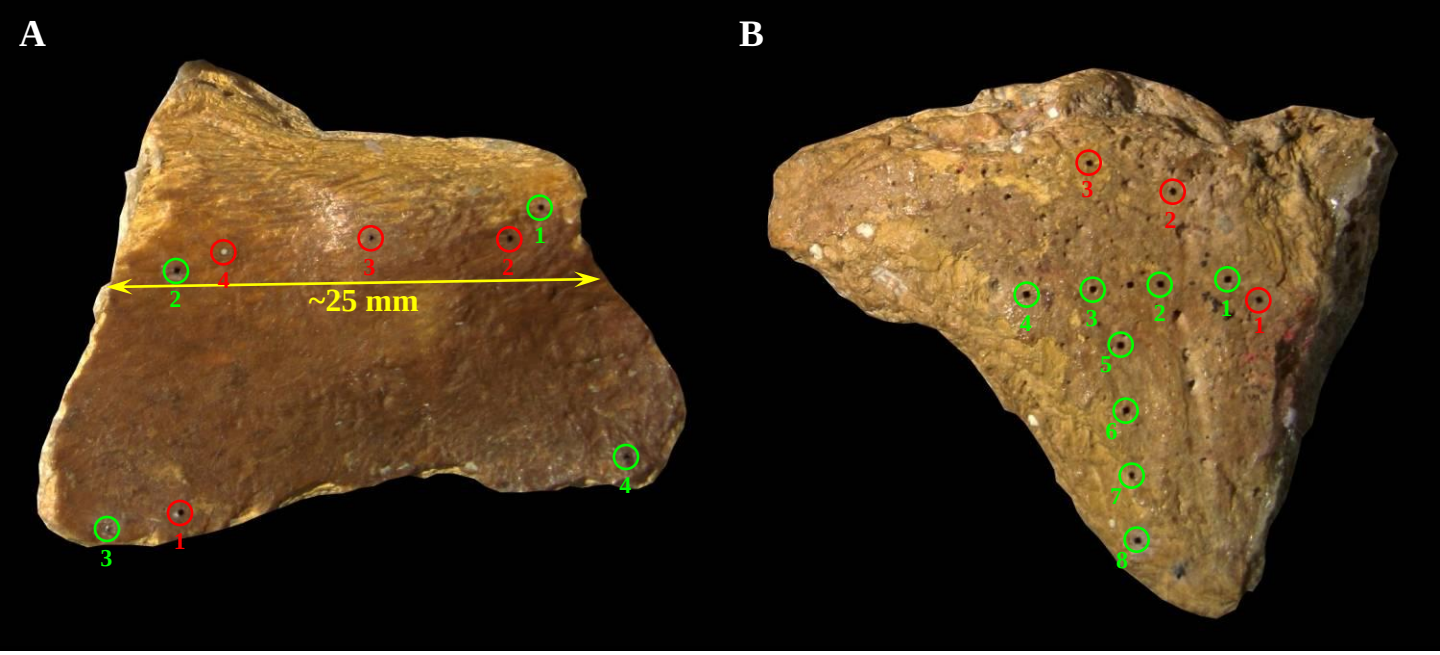

Grün et al. Extended Data Figure 9

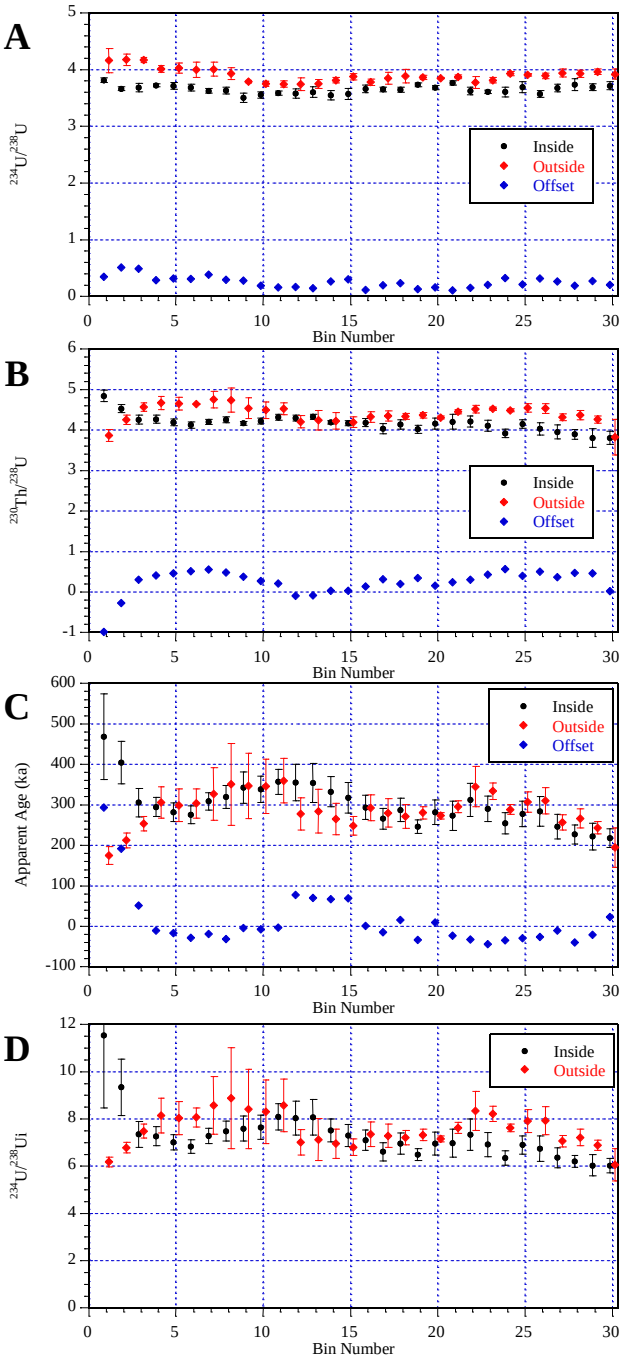

Grün et al. Extended Data Figure 10

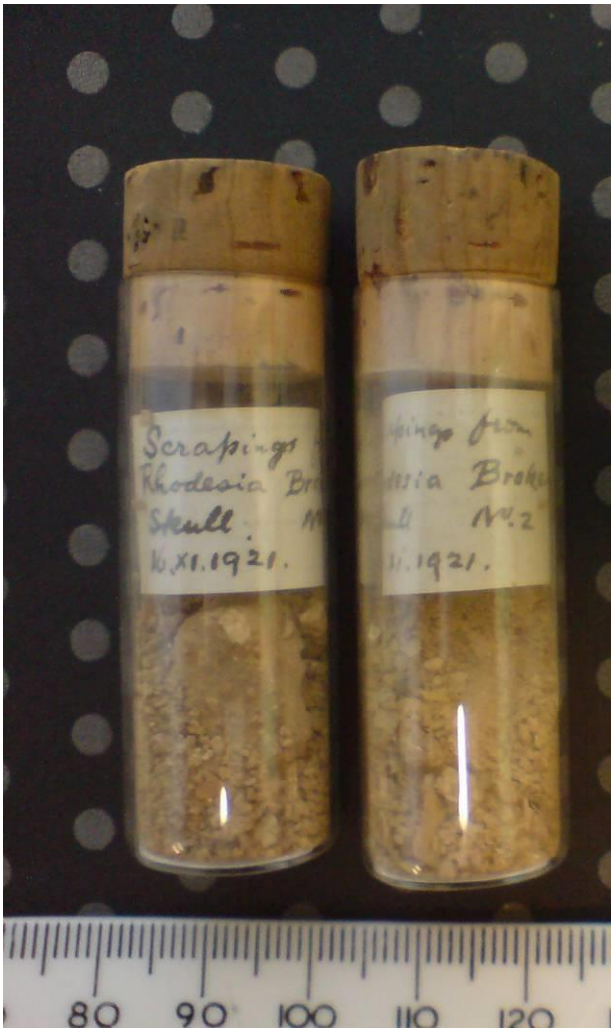

Grün et al. Extended Data Figure 11

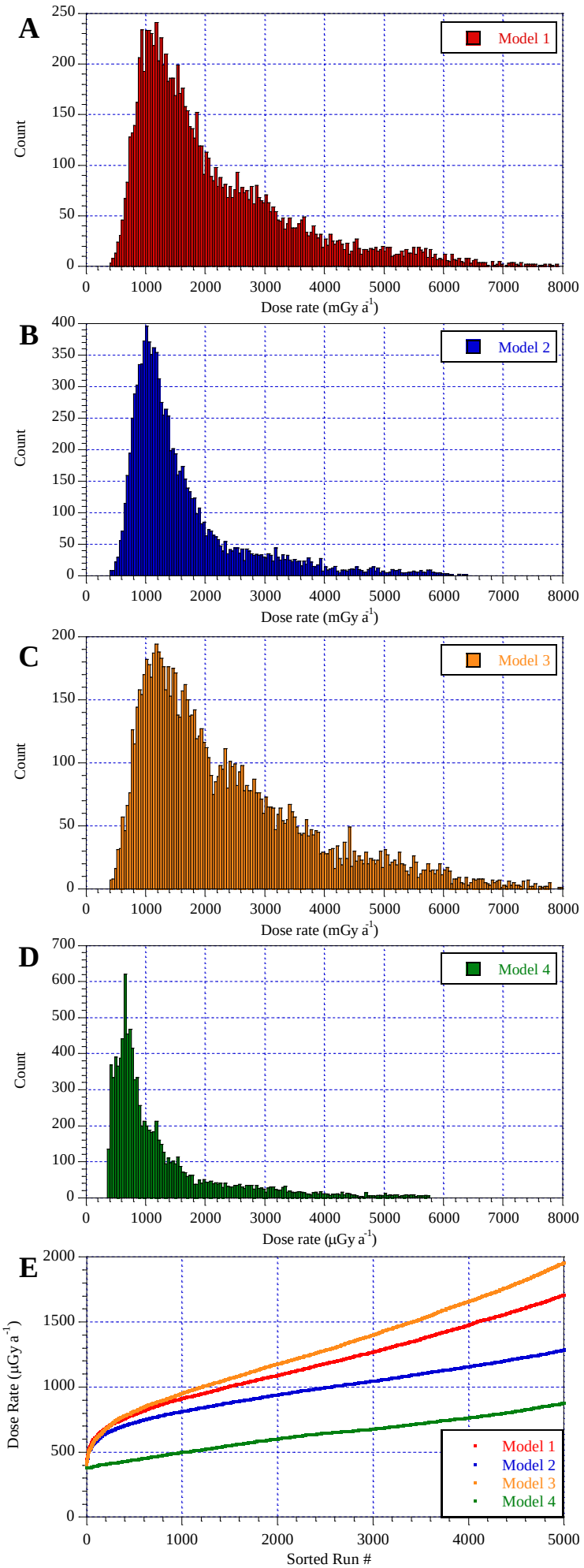

Grün et al. Extended Data Figure 12